TURUN YLIOPISTON JULKAISUJA
ANNALES UNIVERSITATIS TURKUENSIS

SARJA - SER. A I OSA - TOM. 425

ASTRONOMICA - CHEMICA - PHYSICA - MATHEMATICA

MULTIFREQUENCY VLBI OBSERVATIONS OF SELECTED ACTIVE GALACTIC NUCLEI

by

Elizaveta Rastorgueva

TURUN YLIOPISTO
UNIVERSITY OF TURKU
Turku 2011

From

Department of Physics and Astronomy
University of Turku
FI-20014 Turku
Finland

Supervised by

Dr. Kaj Wiik
Department of Physics and Astronomy
University of Turku
Finland

Reviewed by

Dr. Anne Lähteenmäki
Metsähovi Radio Observatory
Aalto University
Finland

Dr. Philip Edwards
Australia Telescope National Facility
CSIRO
Australia

Opponent

Dr. Svetlana Jorstad
Institute for Astrophysical Research
Boston University
USA

ISBN ISBN 978-951-29-4714-0 (PRINT)
ISBN ISBN 978-951-29-4715-7 (PDF)
ISSN 0082-7002
Painosalama - Turku, Finland 2011

Acknowledgements

There are many people who made my journey along this long and winding road possible and, at some moments, even enjoyable. Here, I try to acknowledge as many as can fit in the page, and even more.

First of all, I want to thank my parents. Both of them, for their patience and moral strength to endure me as a child and teenager, and specifically, my mommy - for her unconditional love and never-ending faith in me, and my daddy - for planting in me curiosity and the interest for exploration of the Universe, and for showing me how much fun and joy doing science can be, regardless of the salary.

Next, I want to express gratitude to my supervisors Dr. Kaj Wiik and Prof. Esko Valtaoja, for showing me what is the real everyday scientific work is, for their guidance and help in the process of learning and research. I want to thank the pre-examiners of my thesis Dr. Anne Lähteenmäki and Dr. Philip Edwards for their useful comments and positive evaluation, and Dr. Svetlana Jorstad for agreeing on being my opponent at the public defense.

I also want to thank my research collaborators and instructors, who were inspiring and full of ideas. From them I learned how to choose the right direction of work, and how to arrange results in a scientific publication. They also taught me to involve a proper degree of imagination in the scientific work.

I want to thank my colleagues from Tuorla Observatory and Metsähovi Radio Observatory for creating an inspiring scientific environment. The administrative staff of the Department of Physics and Astronomy of the University of Turku helped me to do all the bureaucracy related to my studies quickly and easily, and I am very grateful to them, too.

The Academy of Finland, the Graduate School of Physics and Astronomy, the University of Turku Foundation and Väisälä Foundation provided financial support during the years of my studies, including travel grants. I want to thank all people involved in this process.

A special thank goes to my colleagues from the Finnish Astronomical Society for the unforgettable experience of being on the board for four years.

I want to thank also all my teachers from Moscow State University, Lebedev

Physics Institute, the University of Turku, and numerous summerschools for introducing me to the exciting world of Physics and Mathematics, and for showing me the plethora of methods that are used in science to pierce the darkness of the unknown and to find the truth.

I want to thank all my good friends. Thank you, guys and girls, for exciting discussions about life, science, Universe and everything, and for all the fun we had together during these years. Special thanks go to Tommi Vornanen, Dr. Esko Gardner, Dr. Alessandro Foi for the language corrections. Also, thanks to Dr. Alessandro Foi for his kindness, support, advice and inspiration to keep on track even in the moments of desperation. Thanks to Dr. Carolin Villforth for the practical advice.

I also have a big gratitude to the very country Suomi, to its nature and people, for making it so fantastic to live in.

My special thanks go to my Master thesis supervisor Dr. Denise Gabuzda, my ‘mother’ in science. She introduced me to AGN research, VLBI science, and has shown me what a life in Academia is, with all its virtues and downsides. She is a role model for me as a successful female scientist, a great person, a caring friend and a very independent thinker. This thesis is dedicated to her.

Elizaveta Rastorgueva,
Kylmälä, 2011

Contents

Abstract

In this dissertation, active galactic nuclei (AGN) are discussed, as they are seen with the high-resolution radio-astronomical technique called Very Long Baseline Interferometry (VLBI). This observational technique provides very high angular resolution ($\leq 10^{-3''}$ = 1 milliarcsecond). VLBI observations, performed at different radio frequencies (multi-frequency VLBI), allow to penetrate deep into the core of an AGN to reveal an otherwise obscured inner part of the jet and the vicinity of the AGN's central engine. Multi-frequency VLBI data are used to scrutinize the structure and evolution of the jet, as well as the distribution of the polarized emission. These data can help to derive the properties of the plasma and the magnetic field, and to provide constraints to the jet composition and the parameters of emission mechanisms. Also VLBI data can be used for testing the possible physical processes in the jet by comparing observational results with results of numerical simulations.

The work presented in this thesis contributes to different aspects of AGN physics studies, as well as to the methodology of VLBI data reduction. In particular, Paper I reports evidence of optical and radio emission of AGN coming from the same region in the inner jet. This result was obtained via simultaneous observations of linear polarization in the optical and in radio using VLBI technique of a sample of AGN. Papers II and III describe, in detail, the jet kinematics of the blazar 0716+714, based on multi-frequency data, and reveal a peculiar kinematic pattern: plasma in the inner jet appears to move substantially faster that that in the large-scale jet. This peculiarity is explained by the jet bending, in Paper III. Also, Paper III presents a test of the new imaging technique for VLBI data, the Generalized Maximum Entropy Method (GMEM), with the observed (not simulated) data and compares its results with the conventional imaging. Papers IV and V report the results of observations of the circularly polarized (CP) emission in AGN at small spatial scales. In particular, Paper IV presents values of the core CP for 41 AGN at 15, 22 and 43 GHz, obtained with the help of the standard Gain transfer (GT) method, which was previously developed by D. Homan and J. Wardle for the calibration of multi-source VLBI observations. This method was

developed for long multi-source observations, when many AGN are observed in a single VLBI run. In contrast, in Paper V, an attempt is made to apply the GT method to single-source VLBI observations. In such observations, the object list would include only a few sources: a target source and two or three calibrators, and it lasts much shorter than the multi-source experiment. For the CP calibration of a single-source observation, it is necessary to have a source with zero or known CP as one of the calibrators. If the archival observations included such a source to the list of calibrators, the GT could also be used for the archival data, increasing a list of known AGN with the CP at small spatial scale. Paper V contains also calculation of contributions of different sourced of errors to the uncertainty of the final result, and presents the first results for the blazar 0716+714.

List of papers

I Evidence for cospatial optical and radio polarized emission in active galactic nuclei,
D.C. Gabuzda, ***E.A. Rastorgueva***, P.S. Smith, and S.P. O'Sullivan, MNRAS **369**, 1596 (2006).

II Multi-frequency VLBA study of the blazar S5 0716+714 during the active state in 2004. I. Inner jet kinematics,
E.A. Rastorgueva, K. Wiik, T. Savolainen, L.O. Takalo, E. Valtaoja, Y.N. Vetukhnovskaya, and K.V. Sokolovsky, A&A **494**, 5 (2009) [arXiv:0812.1156].

III Multifrequency VLBA study of the blazar S5 0716+714 during the active state in 2004. II. Large-scale jet kinematics and the comparison of the different methods of VLBI data imaging as applied to kinematic studies of AGN,
E.A. Rastorgueva, A.T. Bajkova, K. Wiik, E. Valtaoja, L.O. Takalo, Y.N. Vetukhnovskaya, and M. Mahmud, A&A **529**, 2 (2011) [arXiv:1102.0409].

IV The 15-43 GHz parsec-scale circular polarization of 41 active galactic nuclei,
V.M. Vitrishchak, D.C. Gabuzda, J.C. Algaba, ***E.A. Rastorgueva***, S.P. O'Sullivan, and A. O'Dowd, MNRAS **391**, 124-135 (2008) [arXiv:0809.2556].

V Multifrequency VLBA study of the blazar S5 0716+714 during the active state in 2004.III. Detection of the variable circular polarization on the parsec scale,
E.A. Rastorgueva, V.M. Vitrishchak, and K. Wiik, submitted [1] to A&A.

[1] Final published version of the paper may differ from the one presented in this thesis

List of abbreviations

3C / 3CR - third Cambridge catalogue of radio sources / same, revised version
AGN - active galactic nucleus / active galactic nuclei
AIPS - Astronomical Image Processing System, data reduction package
ATCA - Australia Telescope Compact Array
BLR - broad line region
CP - circular polarization
EIC - external inverse Compton
EVPA - electric vector position angle
FOV - field of view
FRI / FRII - Fanaroff-Riley class I / class II
FSRQ - flat spectrum radio quasar
FWHM - full width half maximum
GPS - Global Positioning System
GRB - gamma-ray burst
GT - gain transfer method
LMMSE - Linear Minimum Mean Square Error
LP - linear polarization
MEM - Maximum Entropy Method
MHD - magnetohydrodynamics
NLR - narrow line region
NNLS - Non Negative Linear Least Squares
NRAO - National Radio Astronomy Observatory (USA)
PSF - point spread function
SED - spectral energy distribution
SMBH - super-massive black hole
SSC - synchrotron self-Compton
UTC - Coordinated Universal Time
VLBI - very long baseline interferometry
VLA - Very Large Array
YSO - young stellar object

Chapter 1

Introduction

Galaxies are the cosmological building blocks of the Universe. They are the oldest ordered structures, which were formed by growth of primordial fluctuations in the early Universe. The dark matter formed clumps in the denser areas, which gravitationally attracted gas. These seed clouds compressed under the gravitational force and thus formed the first galaxies.

With the naked eye, assuming the limiting magnitude of six, only few nearby galaxies are visible: Andromeda Galaxy (M31, NGC 224), Large and Small (NGC 292) Magellanic Clouds, Triangulum Galaxy (M33, NGC 598). Under perfect observing conditions, two fainter galaxies may also be seen: Centaurus A (NGC 5128) and Bode's Galaxy (M81, NGC 3031). They appear on the sky as small diffuse objects, and historically were called *nebulae* (not to be confused with the contemporary astrophysical use of the term 'nebulae', which is reserved for clouds of gas and dust residing in the Galaxy). With the help of a simple optical telescope, one can see more of the fainter galaxies. The closest of them are also resolved, but some are so far away that even with the big telescope they look like bright points, and sometimes they are difficult to distinguish from other celestial objects, like stars or asteroids. Absence of the rapid motion on the sky plane rules out asteroids. However, the task of distinguishing distant galaxies from the stars is more difficult, only multi-wavelength photometry or/and spectroscopic observations can help. Just to give a hint of the actual numbers, the deepest image of the Universe, the Hubble Ultra-Deep Field, which was taken in 2003 of a small (200×200 arcminutes) region in the constellation of Fornax, revealed approximately 10 000 galaxies up to redshift of $z > 6$ (Beckwith et al., 2006)

Most, if not all, galaxies host supermassive black holes (SMBHs) in their centers. Masses of those black holes are equivalent to billions of those of the Sun (Ferrarese & Ford, 2005). From the surface of a black hole even the light is not able to escape, which makes them invisible for the direct observation with the

telescope. Positioned in the center of a galaxy, SMBHs govern the motion of the stars and gas around it. Observing the stars motion and acceleration, one can find a mass and location of the central black hole, as it was done for the Milky Way in Ghez et al. (1998, 2000). In the distant galaxies, where nuclear star clusters are not resolved, spectroscopic velocities of gas and/or luminosity of the bulge in the center of galaxy are used for this purpose.

Most of the galaxies are called 'normal', which means that their total brightness is merely made up of emission contributions from the stars, gas and dust that populate the galaxy. However, in some galaxies the central part is substantially brighter than the starry outskirts, and the matter moves faster and faster the closer it is to the center. The long history of observations and theoretical studies of these objects suggested that the SMBH in the center of some galaxies use to 'go wild' and started to consume violently nearby gas, dust and stars. The matter is pulled closer to the SMBH by the gravitational force, and in the immediate vicinity of the SMBH it falls onto it, forming a rapidly rotating hot disc. This process is called *disc accretion*. The *accretion disc*, which is formed in this process, emits a lot of radiation in the broad electromagnetic spectrum. The galaxies, undergoing this process, are called *active*. Sometimes the bright nucleus (the *active galactic nucleus*, AGN) is the only component of galaxy which could be seen from the Earth. It happens either when it is so bright that it outshines all other sources of radiation in the galaxy, or when the object is far away from the Earth, and the light from the stars does not reach the observer, likely a combination of both reasons. These distant objects are called *quasars*, and some particular of them are studied in this thesis.

Observational properties of AGN suggested that they are very powerful sources of energy confined in a very small space. To give approximate size of the AGN central engine, the event horizon of a Schwarzschild black hole that has the mass $M_{\rm BH}$ (*Schwarzschild radius* $r_{\rm S}$), is

$$r_{\rm g} = \frac{2GM_{\rm BH}}{c^2} \approx 3\times10^5 \left(\frac{M_{\rm BH}}{M_\odot}\right) cm = 2\times10^{-8}\left(\frac{M_{\rm BH}}{M_\odot}\right) AU \ ,$$

where G is the gravitational constant, c is the speed of light and $M_\odot$ is the mass of the Sun (Begelman, Blandford & Rees, 1984; Shapiro & Teukolsky, 2004), which is 2 AU for the typical AGN SMBH of $M_{\rm BH} = 10^8 M_\odot$. According to the basic model of a thin accretion disc by Shakura & Sunyaev (1973), the size of the accretion disc is $6r_{\rm g} < R_{\rm AD} < 30r_{\rm g}$, which is from 12 to 60 AU for the above mentioned SMBH. This size is translated into 10^{-8} - 10^{-7} arcseconds on the sky for a broad

range of redshifts. It makes it clear that a very high angular resolution is needed for the direct observation of the central regions of AGN. The radio-astronomical technique called Very Long Baseline Interferometry (VLBI) provides the highest possible angular resolution of up to 5×10^{-5} arcseconds $= 50$ milliarcseconds for the present day. It is not yet enough to resolve directly the accretion disc, but it allows to observe directly regions of AGN very close to the center.

If the nucleus of the Milky Way or a close-by galaxy becomes active, it will be dangerous, perhaps even fatal, for the life on Earth or any other planet in the neighborhood (provided it exists). It is known that 0.2 % of the galaxies in the immediate neighborhood of the Milky Way ($z < 0.125$) are active, and this fraction rises to 4 % in the larger radius of $z < 0.7$ around the Galaxy (Haggard et al., 2010). There are many factors that determine activity: environment, in which galaxy was formed, interaction with neighbors, type, age, redshift, etc. However, there is not yet a good understanding what are the key parameters for triggering the activity in a normal galaxy. Study of individual AGN helps to understand the nature of the phenomenon deeper, and thus contribute to the overall picture.

The outline of this thesis is as follows. The VLBI technique, its capabilities and limitations are described in Chapter 2 of the introductory part. Chapter 3 is dedicated to the AGN phenomenon in general, including history of their discovery and observations, short explanation of the physical model and their observational behavior. In the radio domain, AGN are dominated by the non-thermal emission from the relativistic jet. Chapter 4 is concentrated on these jets. It covers observational phenomenology of jets, the current physical paradigm, and the way how physical parameters could be obtained/constrained by observations. These aspects of AGN research are narrowed down in five papers that can be found in the second part of the thesis. Each of the articles presents results of a distinct project, even though some of them include the same observational data.

Chapter 2

Very Long Baseline Interferometry

2.1 Resolution in astronomy

The history of observational astronomy is a rush for the angular resolution. Angular resolution in astronomy is restricted by the diffraction limit, which is defined by the ratio λ/D, where λ is the wavelength of observation and D is the diameter of the telescope. This formula is universal and can be applied to the whole electromagnetic range. Historically, optical astronomy developed first as an observational technique. The eye sensitivity curve has its maximum around the wavelength $\lambda = 5550$ Å, thus the theoretical limit for the resolution of an optical telescope with a mirror diameter of 1 m is $0.1''$ in visible light, and for a telescope with an aperture of 10 m (such as the Gran Telescopio Canarias on the Canary Islands, Spain, or the Keck telescopes in Hawaii, USA) the resolution would be $0.01''$ or 10 milliarcseconds (mas). The diffraction limit is reached at the large contemporary telescopes, where adaptive optics corrects for the influence of the atmosphere, otherwise atmospheric turbulence limits resolution to as much as $1''$.

However, atmospheric turbulence can also be used to improve the resolution, as in the observational technique called *speckle imaging*. During a short time interval, the turbulent atmosphere stays relatively stable, so images of the target source taken with very short (10-100 ms) exposures, represent the instant atmospheric seeing. Such images are called *speckle patterns*. Multiple speckle patterns of the target source are processed together, for example, lined up by the brightest pixel and added, as in the *shift-and-add* method, or processed using Fourier analysis, as in the variations of *speckle interferometry* (e.g., Labeyrie, 1970). Speckle imaging allows relatively small telescopes to reach the diffraction limit. However, due to

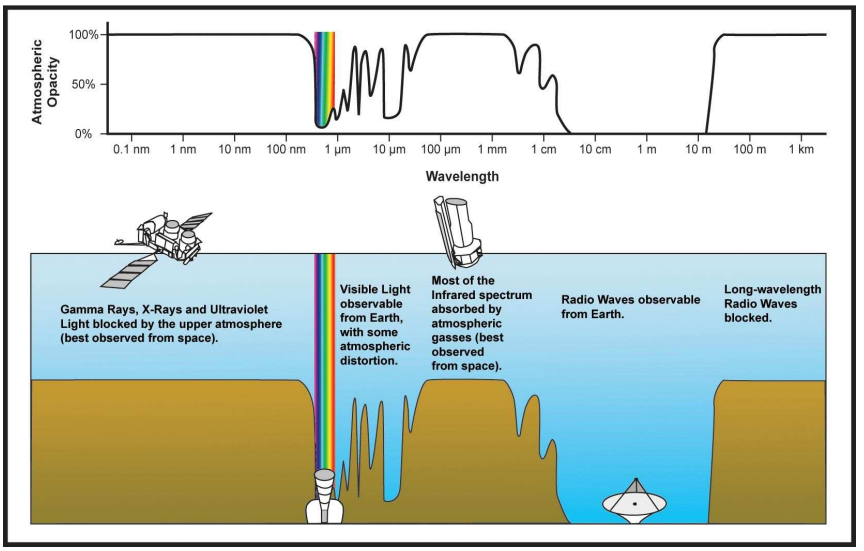

Figure 2.1: The transparency of the Earth atmosphere for cosmic radiation. Credit: NASA/IPAC.

the short exposures used in this technique, it is limited to the brightest sources.

Radio astronomy operates at wavelengths from millimeters to ten meters, in the radio bands which pass through the Earth's atmosphere (see Fig. 2.1). There exist many different types of radio telescopes including various dipole arrays, linear antennae, feed focal-plane arrays, but the most popular type, nowadays, is the *fully steerable parabolic reflector*, having the receiver in the primary or secondary focus. Due to the advantages in design and manufacturing, paraboloids are able to observe at the shortest wavelengths of the radio range. For the centimeter wavelength, the typical diameter of an antenna is 25 meters, the maximum currently being 100 m (Green Bank Telescope, Effelsberg Radio Telescope). Resolution in this case is $\sim 1'$, $20''$ at best, which is 1000 times less than the best optical resolution. However, steady development in design and the technology of manufacturing of electronic components, and their growing effectiveness, led to the development of *radio interferometry*. Radio interferometry is a radio astronomical observational technique which allows not only to catch up with optical astronomy, in terms of resolution, but rather to overtake it.

Radio astronomy, as an observational technique, was born just before World War II. The first radio emission from an astronomical object, the Milky Way, was

serendipitously discovered by Karl Jansky in 1933. In 1937, Grote Reber, inspired by Jansky's discovery, built a radio telescope and started radio astronomical observations. However, as science, radio astronomy shaped up only in the late 1940s. The resolution problem was clear from the very beginning, and attempts were made to overcome it. This led to the invention of the two-element radio interferometer in 1946. The first interferometer was built by Martin Ryle and D. Vonberg, for the observations of solar radio emission (Ryle & Vonberg, 1946). It consisted of two dipoles.

In interferometry, the angular resolution of the system depends not on the single telescope aperture, but on the distance between elements, B, the so-called *baseline*. Thus, increasing the distance between the elements of an interferometer can improve the angular resolution of the system.

Already the early two-element interferometers measured the angular sizes of astronomical objects. They observed change in the intensity of the interference pattern as a function of the distance between the antennas, while they were gradually moved closer to each other. This was done in order to find a limit in the spatial coherence and to compare it with the values which were predicted by the model of the intensity distribution. In this way, the size of the source can be constrained. Later, more sophisticated interferometers begun to utilize a technique called *aperture synthesis*, or *synthesis imaging*. An aperture synthesis array consists of many telescopes that are connected pairwise in order to form several baselines, which are used simultaneously. One baseline interferometer with a fixed distance between antennas can measure the brightness of the source at only one spatial scale, or so called *spatial frequency*. Aperture synthesis array must have baselines of different lengths, so it can measure many spatial frequencies simultaneously and form an *image* of the observed object with details of different sizes: the image would contain the structure elements, whose angular size corresponds to each spatial frequency available. The use of Earth's rotation increases the number of available spatial frequencies, due to projection.

However, several new astronomical discoveries revealed an existence of object smaller than the current resolution limit. First, rapid time variations of quasar brightness, at the timescale of days, suggested that the size of the region in the source, where the radiation was produced, was of the order of several light days, which translates into the apparent sizes of less than milliarcsecond on the sky plane. Scintillations of the radio emission from quasars due to its propagation through the turbulent plasma of the solar corona suggested the same size for the emitting region. Finally, the observations of OH-masers with connected element interferometry could not resolve them. These observations brought up a need for

the increase of resolution beyond the values provided by the connected element interferometry, hence, longer baselines were needed. It led to the development of the new technique called *Very Long Baseline Interferometry*, or VLBI. In VLBI, baselines reach length of thousands of kilometers. Thus, VLBI antennas operate independently, there is no direct connection between them.

In this thesis, I follow the description of the basics of interferometry as given in the book 'Tools of Radio Astronomy' (Wilson, Rohlfs & Hüttemeister, 2009). For the additional questions, which need more thorough explanations, I refer to the book 'An Introduction to Radio Astronomy' (Burke & Graham-Smith, 2010), and for the more detailed technical descriptions of the certain aspects of the radio interferometry and aperture synthesis I refer to the book by 'Interferometry and Synthesis in Radio Astronomy' (Thompson, Moran & Swenson, 2004). I don't refer to these books further in the text since the theory given in this chapter is well established, however, in many cases I give references for discussion of some specific topics.

2.2 Two-element interferometer

In this section I will introduce the simplified concept of interferometry as applied to radio astronomy, though the same principles are relevant for optical interferometry as well. The theory of interferometry presented in this chapter is expounded in a case of monochromatic radiation, propagating in vacuum. However, this approximation could still be used in the case of real observations, since the real source radiation could be considered monochromatic within the *coherence time* t_c, for which the rms phase error is one radian (Thompson, Moran & Swenson, 2004). Within the coherence time the amplitude of the signal remains roughly constant. The propagation of radiation through matter is not considered in this section in order to avoid taking into account the influence of medium on the amplitude and phase of the signal. Also, it is implied that the observed source is so far from the Earth so that the wavefront is flat on the scale of the longest baseline of the interferometer (a so called *far field* source).

The two-element interferometer is a basic element of a radio interferometer of any complexity. The two antennas A_1 and A_2, separated by the distance B, called baseline, detect radio emission from the source. The flat wavefront reaches both telescopes at two time instants t_1 and t_2. If the source zenith angle is Θ, then the

difference in the path of the wavefront is $B\sin\Theta$, and the time delay is:

$$\tau = t_2 - t_1 = \frac{B\sin\Theta}{c} , \tag{2.1}$$

where c is the speed of light. The value of the projection of the baseline onto the sky plane defines the spatial frequency which is sampled by the given baseline at a given time instant. It can be calculated according to the formula $(B\cos\Theta)$, which makes it clear that the spatial frequency is a function of baseline length and time, since the source is moving on the sky plane during the observing session. Therefore, if the Earth motion is used in interferometry observations, it allows one to observe more spatial frequencies with respect to the observation in the snapshot mode.

2.2.1 Coherence function

A radio telescope acquires the electrical component of the electromagnetic field, which changes as a periodic function of time. The measured quantity is the voltage, which is induced by the incoming electric field at the antenna. The output voltage is proportional to the magnitude of the input electric field, if one does not take into account instrumental effects:

$$U_{1cos} \propto E\cos\omega t , \qquad U_{2cos} \propto E\cos\omega(t-\tau) , \tag{2.2}$$

for antennas A_1 and A_2, respectively. E is the amplitude of the electric field, ω is an angular frequency and t is time. If the phase difference of $\pi/2$ is introduced to the output signal, the induced voltage will have a *sin* form:

$$U_{1sin} \propto E\sin\omega t , \qquad U_{2sin} \propto E\sin\omega(t-\tau) . \tag{2.3}$$

The *sin* and *cos* outputs from each antenna are combined in a way that the formula for antenna output has complex form:

$$\begin{aligned} U_1 &\propto E(\cos\omega t + i\sin\omega t) = Ee^{i\omega t} \\ U_2 &\propto E(\cos\omega(t-\tau) + i\sin\omega(t-\tau)) = Ee^{i\omega(t-\tau)} . \end{aligned} \tag{2.4}$$

For the electric field $E(P,t)$ in two different points P_1 and P_2 and two different instants of time t_1 and t_2, one can define the *spatio-temporal coherence function*

(or simply coherence function):

$$V(P_1,t_1,P_2,t_2) = < E(P_1,t_1)E^*(P_2,t_2) > , \tag{2.5}$$

where angle brackets denote the average over a time interval, and asterisk here and throughout this chapter denotes the complex conjugation. The averaging time interval is assumed to be long compared to the period of field oscillation. In practice, the measured correlator output of two antennas corresponds to the coherence function: voltages from the two receivers are transferred to the *correlator*, a powerful computer which multiplies signals and averages the product over time:

$$< U_1 U_2^* > \propto V(P_1,t_1,P_2,t_1+\tau) = \frac{E^2}{T}\int_0^T e^{i\omega t}e^{-i\omega(t-\tau)}dt \ . \tag{2.6}$$

Since the averaging time T is much longer than the period of the field oscillation, the average is close to the average over a single full period. As a result,

$$< U_1 U_2^* > = R(\tau) \propto \frac{1}{2}E^2 e^{i\omega\tau} \ , \tag{2.7}$$

where $R(\tau)$ is a *mutual coherence function*, which is closely related to the coherence function $V(P_1,t_1,P_2,t_2)$. $R(\tau)$ depends on the delay between the arrival of the wavefront to the antennas of the given baseline, and, therefore, on the orientation of the baseline with respect to the wavefront. When the baseline is parallel to the wavefront, $t_1 = t_2$, so $\tau = 0$ and $R(\tau)$ reaches its maximum value. If one considers an electric field from a point source, it arrives to both antennas in phase, creating the main interference maximum at the output of the correlator. The *central fringe* is defined as a point on the sky, such that a point source placed in it causes an interference maximum in the correlator output from the baseline. The position of the central fringe is defined with respect to the given baseline, and it is not unique. The central fringe also defines the *phase tracking center*. Interference of the two incoming waves at the given baseline depends on the source position on the sky: since τ depends on the angle between the direction to the source and to the phase tracking center, the interference of the correlated signal in the output is 'mapped' into the sky plane, forming a pattern, which is a periodical function of the angular distance of the object from the phase tracking center. This pattern is called *the fringe*. Since the position of the source on the sky is changing with time, due to the Earth's rotation, or, in another reference frame, the position of a baseline is changing with respect to the source on the sky. For the observer placed

on the Earth's surface, fringes are slowly moving across the sky. Therefore, one can measure $R(\tau)$ as a function of time.

2.2.2 Possibility of imaging of extended sources

In practice, in radio interferometry, one mainly deals with extended sources, which produce a quasi-monochromatic wave field. According to the van Cittert-Zernike theorem, for a spatially incoherent source in the far field, the value of the spatial coherence function $V_s(\mathbf{r}) \equiv V(P_1,t_1,P_2,t_1)$, normalized to its value for the zero distance $V_s(\mathbf{0}) = V(P_1,t_1,P_1,t_1)$, is equal to the normalized Fourier transform of the source brightness distribution:

$$\frac{V_s(\mathbf{r})}{V_s(\mathbf{0})} = \frac{\int\limits_{\Omega} I(\mathbf{s}) e^{-i\omega \mathbf{s}\dot{\mathbf{r}}/c} d\mathbf{s}}{\int\limits_{\Omega} I(\mathbf{s}) d\mathbf{s}} \,, \tag{2.8}$$

where $\mathbf{s}$ is a unit vector, pointing to the source, $\mathbf{r}$ is a vector distance between two points P_1 and P_2, Ω is the solid angle of the source and $I(\mathbf{s})$ is a source brightness distribution. Detailed discussion of this theorem exceeds the scope of this thesis. However it can be found, for example, in Thompson, Moran & Swenson (2004), Chapter 14, together with the notes on its importance for interferometry.

For a small source, we can write the relation (2.8) in a coordinate form:

$$\frac{V_s(u,v)}{V_s(0,0)} = \frac{\iint I(l,m) e^{-i\omega(ul+vm)/c} dl dm}{\iint I(l,m) dl dm} \,, \tag{2.9}$$

where (l,m) are the angular coordinates on the sky plane with respect to the phase tracking center, and (u,v) are the baseline coordinates, which are perpendicular to the vector $\mathbf{s_0} = (0,0,1)$, pointing to the phase tracking center. Coordinates (u,v) are traditionally measured in wavelengths. The normalization factor in equation (2.9) is taken into account during the calibration of the measured value of the spatial coherence function. It makes sense to label this normalized value, which is also known as *complex visibility*, as $V(u,v)$.

In practice, each antenna has its own sensitivity pattern, depending on the angle with respect to the direction perpendicular to the antenna, the so called *primary beam* $A(l,m)$. The source intensity distribution is modulated by the antenna

response:

$$V(u,v) = \iint A(l,m)I(l,m)e^{-i\omega(ul+vm)/c}dldm\ . \tag{2.10}$$

The primary beam response of each individual antenna in the interferometer is nearly zero everywhere, except close to the pointing center, and, therefore, it restricts the field of view (FOV) of the interferometer. The signal is compensated for the geometrical time delay τ_g that introduces a visibility phase term equal to $\omega\tau_g$, which centers the FOV at the phase tracking center. If the extended source takes only a small fraction of the FOV, as it is for most active galactic nuclei, all previous considerations hold.

Since a Fourier transform is invertible, the sky brightness distribution can be recovered from the measured $(u,v)-$plane distribution of the complex visibility by taking an inverse Fourier transform of the expression (2.9):

$$I(l,m) = \iint V(u,v)e^{i\omega(ul+vm)/c}dudv\ . \tag{2.11}$$

This is the main equation of interferometry, which illustrates the possibility to build an image of an extended source.

2.2.3 Observations in the limited frequency band

In this section, I consider the frequency of the electromagnetic radiation ν, in contrast to the angular frequency ω used in previous sections. These two quantities are connected by the expression $\omega = 2\pi\nu$.

In reality, observations are not monochromatic, as was assumed in section 2.2, but are carried out within a narrow *frequency band* $\Delta\nu$. Thus, the complex visibility is also a function of frequency $V(u,v,\nu)$ within the frequency band. In practice, the observed frequency band is split into a number of narrow spectral channels, and, for each baseline, signals from corresponding channels are correlated. Frequency channels are filtered out by taking the Fourier transform of the signal in the time domain:

$$V(u,v,\nu) = \int V(u,v,\tau)e^{i2\pi\tau\nu}d\tau\ . \tag{2.12}$$

There are two different types of the *spectral correlators*, namely FX and XF correlators, where "F" stands for the Fourier transform and "X" - for multiplication, and the order of those procedures is reflected in the name. In the FX cor-

relator, band-limited signals from the two antenna outputs are first Fourier transformed in the time domain in order to obtain the frequency spectrum. This procedure allows one to create a number of narrow-band outputs from each antenna, i.e. the Fourier transform serves as a frequency filter. The spectral visibility is then formed by multiplying each of these spectral components of one antenna with the corresponding spectral components of another. These products are then integrated over time to get an estimate of the correlation function. For continuum observations, the visibility measured for all spectral components can be averaged after the bandpass calibration (see Section 2.3.2).

In the XF correlator, in contrast, a variable time delay τ is introduced to one of the antenna outputs, lets call this antenna 1. The output of antenna 1 for each time delay is multiplied by the (unaltered) output of antenna 2 and integrated over time. This creates a cross-correlation measured as a function of τ. Then the Fourier transformaton is performed in order to obtain the cross-correlation spectrum.

2.3 Aperture Synthesis and VLBI

Aperture synthesis is a general name for an interferometric observational and data reduction technique, which allows one to obtain a map of the intensity distribution of a source using an array of telescopes. Equation (2.11) is key for synthesis imaging. The idea of this technique may seem relatively easy, consisting only of the inversion of the visibility function, defined on the (u,v)-plane, into the source brightness distribution function on the sky plane. However, the procedure of inversion is not trivial. Numerous instrumental and environmental effects have an effect on the data, and they need to be taken into account for the reliable restoration of a source map. In this chapter, I will describe main sources of errors and tell about data reduction strategies which are used to disentangle data from the error in very long baseline interferometry.

VLBI differs from other interferometric techniques because antennas are located thousands of kilometers from each other, and there is no phase connection between them. In the recent years, there have been a number of *eVLBI* projects, which connect individual VLBI antennas to a correlator using broad-band internet lines in order to be able to perform correlation in real time. In the most of VLBI arrays, however, the signal from each antenna is digitized and recorded on the spot to a hard drive pack, and after the observing session the pack is shipped to the correlator, where the data are resynchronized and multiplied pairwise according to the time labels, and then averaged. The observer receives only the output

of this whole procedure: correlated visibilities. The process of observation and correlation introduce errors to the data, which have to be calibrated out.

2.3.1 Sources of errors during VLBI observation

Since the visibility is a complex value, it can be expressed in an exponential form:

$$V_{mn} = A_{mn} e^{i\Theta_{mn}} \ , \tag{2.13}$$

where m and n refer to labels (often sequence numbers) of each of the two antennas in the baseline. Amplitude A_{mn} and phase Θ_{mn} are considered separately: different factors cause errors in the amplitude and phase, and they are treated separately in the calibration process. The phase of the visibility is more important for image restoration, since it is responsible for the position of the source on the image plane: error in the amplitude leads to the overall brightness offset of the source, whereas error in the phase leads to the loss of information about the source structure. For example, if the amplitudes are correct, but noise in the phases is comparable with the phase values, one may end up with a uniformly illuminated FOV instead of a point source. In the image analysis, it is useful to remember that phase errors introduce non-symmetrical artifacts on the image, whereas amplitude errors always result in symmetrical features.

Amplitudes

Amplitude errors mostly arise from faulty calibration of the *system temperature* T_{sys} of individual antennas and errors in the determination of the *aperture efficiency* A_{eff}. System temperature and aperture efficiency depend on the radio telescope characteristics, such as surface accuracy, spillover factor, subreflector blockage, illumination, radiation efficiency, pointing accuracy, calibration errors, etc. These factors are not specific to interferometry observations and play a role in single dish observations. The value of the amplitude of the correlator output, the *correlated flux density*, depends on a combination of these factors. For the baseline between antennas i and j it has the following form:

$$S^{c}_{ij} = \rho_{ij} \cdot b \cdot 2k \cdot 10^{26} \sqrt{\frac{T_{\mathrm{sys},i} T_{\mathrm{sys},j}}{A_{\mathrm{eff},i} A_{\mathrm{eff},j}}} \ , \tag{2.14}$$

where ρ_{ij} is a *correlator coefficient*, which is the raw output of the correlator, and it is converted to the correlated flux density by the *a-priori* amplitude calibration.

b is a correlator scaling factor and k is the Boltzmann constant. Correlated flux density is measured in Jansky (1 Jy = $10^{-26}\frac{W}{m^2 Hz}$).

Another factor which plays an important role in radio-astronomical observations is the attenuation of the signal due to atmospheric opacity. Absorption in the atmosphere is a function of source elevation and observation frequency, and it is especially important at the high frequencies ($\geq$ 22GHz) (Burke & Graham-Smith, 2010). Absorption arises from molecular resonances of oxygen, ozone and water vapor. Its influence is especially disruptive for VLBI, since an atmosphere content and source elevation is different at two widely-separated telescope sites, which leads to a non-zero difference between the two signal paths lengths. Atmospheric absorption has one more effect on radio-astronomical observations: it adds an extra component to the antenna temperature, due to thermal radiation from the atmosphere. The path length in the atmosphere is proportional to $\sec z$, where z is a local *zenith distance*, so the total opacity will depend on the source zenith distance. In this section we denote atmospheric opacity with the symbol τ: $\tau = \tau_0 \sec z$, where τ_0 is the opacity at zenith. For the atmosphere having temperature T_0, the system temperature is

$$T_{\rm sys} = T_{\rm rec} + T_0(1 - e^{-\tau_0 \sec z}) \sim T_{\rm rec} + T_0 \tau_0 \sec z, \tag{2.15}$$

where $T_{\rm rec}$ is the temperature of receiver. The system temperature depends almost linearly on $\sec z$, thus, a linear fit to the plot of $T_{\rm sys}$ vs $\sec z$ could be used to determine the receiver temperature and τ_0, which are then used for opacity correction (Moran & Dhawan, 1995).

Phases

At each station of the VLBI array, the incoming signal follows the standard path: after detection with an antenna, the signal enters the receiver, where it is amplified at the original frequency by the low-noise amplifier, then translated to an intermediate frequency by combining it to the local oscillator signal in a mixer, which produces a signal at a lower frequency, which is equal to the difference of the original frequency and a frequency of the local oscillator. Multiple mixing is used to convert the signal to the lower frequency (*baseband*). After that the signal is digitized: it is sampled within short time intervals, and the resulting bit sequence is broken into blocks which get a time label. The label is later used in the correlator to reconstruct the time series for each antenna. For keeping track of time and generating those time stamps, each VLBI station should be equipped with a very precise

clock, and the clocks at all stations should be synchronized with good accuracy, in order to avoid incorrect time labeling. For the clock synchronization and the local oscillators frequency keeping atomic frequency standards are used. Those frequency standards are very stable: their drift rate, i.e. the fractional frequency change per day, is only about 10^{-12}-10^{-15} (Thompson, Moran & Swenson, 2004), so the phase delay slowly increases with time. This error leads to a time error and oscillator frequency error, which are also translated into the phase error of the resulting complex visibility function. Also, errors may occur during the correlation, and such noise in the data is baseline-based. It is small, but more difficult to calibrate away (see Section 2.3.4).

In order to keep the center of the FOV at the phase tracking center, the signal from one of antennas in the baseline is compensated for the geometrical time delay τ_g which has a known dependence of time. Bt due to the clock-setting accuracy problems, its determination may not be correct, and it introduces additional time delay. However, in the last years this problem became less acute because of the use of the Global Positioning System (GPS) to determine an antenna's coordinates and clock error with respect to the Coordinated Universal Time (UTC). The accuracy of the relative time error determination is currently in the order of 10 nanoseconds (Thompson, Moran & Swenson, 2004). More phase error is introduced by the fact that two antennas move with slightly different speeds in the direction of the source, causing differential Doppler shifts in the correlated signal. Since VLBI antennas are far away from each other, conditions at their sites could be different during the same observational session, which leads to another time delay, time-variable in an unpredictable manner, caused by the difference of the atmospheric path of the signal at both sites. There are also instrumental-caused time delays which influence the phase (due to, for example, different paths between receiver and the signal-sampling system). The above mentioned error sources create an additive phase error Θ^{e}_{mn} which should be calibrated out in order to obtain the true visibility phase:

$$\Theta^{\mathrm{e}}_{mn} = 2\pi\nu(\nu_{\mathrm{bb}}R_{mn}t - \nu_{\mathrm{lo}}R_{mn}t - \nu_{\mathrm{bb}}(\Delta\tau_{\mathrm{a}} + \Delta\tau_{\mathrm{i}} + \Delta\tau_{\mathrm{g}}) + \Theta^{\mathrm{n}}_{mn}\ , \qquad (2.16)$$

where ν is the frequency of observation, ν_{bb} is the baseband frequency, and ν_{lo} is the frequency of the local oscillator. R_{mn} is the difference in the frequency drift rates of antennas i and j, and $\Delta\tau$ are differences in the time delays caused by the wrong determination of the geometrical time delay τ_{g}, instrumental delay τ_{i} and delay caused by the atmospheric path difference τ_{a}, and Θ^{n}_{mn} is a measurement noise error. Nowadays, the instrumental effects are very small due to advances

in technology, so the atmospheric effects prevail over other causes of the residual phases in the measured visibility function.

2.3.2 *A-priori* calibration

While a VLBI observation itself is carried out by professional observers and technical staff at the observatories in the allocated time, the calibration of the VLBI data is performed after the actual observation by the astronomers themselves. The *a-priori* calibration compensates for the influence of the known factors in order to obtain minimum errors in phases and amplitudes, which are as close as possible to the true values. If there is no special software provided by the VLBI array managers, it is done with the help of the Astronomical Image Processing System (AIPS, Bridle & Greisen, 1994), supported by the National Radio Astronomy Observatory (NRAO) of the USA and distributed for free. For more detailed information on the package and the calibration process please consult 'The AIPS Cookbook' (NRAO, 2010), the newest version of which is freely available at the NRAO web-page.

In the measurement process, the real signal from the source is modulated by the antenna transmission function. Therefore, the measured visibility $V'_{mn}(u,v,t,\nu)$ can be presented as a function of the real visibility $V_{mn}(u,v,t,\nu)$ which is multiplied by the antenna-based complex coefficients called *gains*:

$$V'_{mn}(u,v,t,\nu) = G_m(t,\nu)G^*_n(t,\nu)V_{mn}(u,v,t,\nu)\ . \tag{2.17}$$

Formula 2.17 only includes the antenna-based gain coefficients because the contribution of the baseline-based terms to the amplitude is negligible.

Amplitudes

To calibrate the correlated flux density (2.14), one needs to apply the system temperature and elevation-dependent aperture efficiency of each antenna to the raw data. System temperature is monitored at each station, and aperture efficiency as a function of the source elevation is also measured. This information is provided to the astronomer along with the data. Also, for the high frequency observations (from 15 GHz onwards) the atmospheric opacity should be taken into account. It is calculated from the known temperatures of the atmosphere and the receiver and the measured system temperature.

Phases

All the causes of the phase error in the data, which were listed in section 2.3.1, can be taken into account, to some extent, in the correlator model. The phase error (2.16) has terms depending on both time and frequency, therefore, in order to build a complete correlator model, one has to know the rate of change of the measured visibility phase with respect to both of them. The derivative of the measured visibility phase with respect to time is called *fringe rate*, and with respect to frequency - *delay*. Clock offsets cause residual phase offsets and delays in the data, and different signal paths in the electronic elements cause additional delays, which depend on the baseband frequency. These delays are calibrated either by using the *pulse-cal* system, which injects a pulse-like short-period reference signal in the receiver front end, or by calculating those delays and offsets for a short scan of a strong calibrator source (*phase calibrator*) and then applying them to the whole data set. This is called *a-priori single-band delay* calibration.

After that, there are still residual delays and rates in the data due to the inaccuracy of the correlator model. The correlator calculates the visibility phase as a function of time for each value of a delay from a broad range. For a delay and rate calibration, VLBI data analysts use the *fringe-fitting* procedure, which searches for the fringe maximum in the time-frequency space (the time axis becomes frequency under the Fourier transformation). The searched for parameters are *lag* and *fringe rate*. If such a search is performed in the whole data set, as opposed to the one-baseline search, it is referred to as *global* fringe fitting (Schwab & Cotton, 1983). A comprehensive discussion of the fringe fitting technique and its applications can be found in Cotton (1995).

Bandpass

Due to electronic effects, individual baseband channels can have amplitude and phase variations. These effects are also calibrated by finding the bandpass shape using a strong continuum source (*bandpass calibrator*) and then applying the correction to the rest of the data.

2.3.3 Polarization

Some radiation mechanisms produce polarized emission. For example, both maser and synchrotron radiation are linearly polarized with a small degree of circular polarization. Pulsar radio emission, the origin of which is not known in detail, is

linearly polarized up to 100 %, sometimes with a presence of a circular component as well. Studies of the polarization properties of the radiation are directly connected to the study of the magnetic field in the observed source.

Feeds of radio telescopes detect the polarization of the incident radiation. The receiving system is arranged in a way that it registers two opposite states of polarization, from which the full polarization of the incoming radiation can be recovered. Polarized outputs from a baseline are correlated, and the resulting visibility data contain information about the distribution and the location of the polarized emission within the source. However, the system for radio emission detection and registration is not ideal, and this is also true for polarization. Instrumental polarization of the antenna alters the observed quantities, which, therefore, should be calibrated separately. In this section I remind the reader of the mathematical description of polarization, tell about the polarization sensitivity of an antenna and interferometer, and list VLBI data calibration steps which should be applied to polarization data.

Mathematical description

The emission which can be detected with the help of a telescope is a manifestation of the electric component of electromagnetic radiation. A time-varying electric field has form of a *sin* or *cos* wave, and the electric field vector takes an arbitrary position in space. If the electric vector has a preferred direction, one can tell that *emission is polarized*. The two most important cases are *linear* and *circular* polarization: if the vector can only take a fixed direction in space, the emission is called *fully linearly polarized*, and if the end of the electric vector draws a circle, one talks about *fully circularly polarized* emission. In reality, those two cases are rarely met: emission of a real cosmic source would contain a mix of the unpolarized (with chaotic changes of the position of the electric vector) emission, linearly and circularly polarized emission. The amount of the last two is measured in percent of the total intensity. A general case for the polarization of incoming radiation is shown in Fig. 2.2. In the case of the full linear polarization the ellipse degenerates into a line, and in case of the full circular polarization the ellipse degenerates into a circle. Mathematically, linear polarization could be represented as a sum of two circular polarizations with a phase difference which defines its position angle, and this fact is a key principle for the polarization observations and data reduction in radio astronomy.

In optics, polarization state of the emission is described by four quantities called the *Stokes parameters*: I, Q, U and V. They are defined through the com-

ponents of the radiation field, either projections to the two perpendicular axes x and y, or the two orthogonal circular polarization components, right R and left L. The following formulas describe the polarization state using right and left circular components:

$$\begin{aligned} I &= < E_{\mathrm{R}}^2 > + < E_{\mathrm{L}}^2 > , \\ Q &= 2 < E_{\mathrm{R}} E_{\mathrm{L}} \cos\delta_{\mathrm{RL}} > , \\ U &= 2 < E_{\mathrm{R}} E_{\mathrm{L}} \sin\delta_{\mathrm{RL}} > , \\ V &= < E_{\mathrm{R}}^2 > - < E_{\mathrm{L}}^2 > , \end{aligned} \tag{2.18}$$

where E_R and E_L are the amplitudes of the corresponding radiation field com-

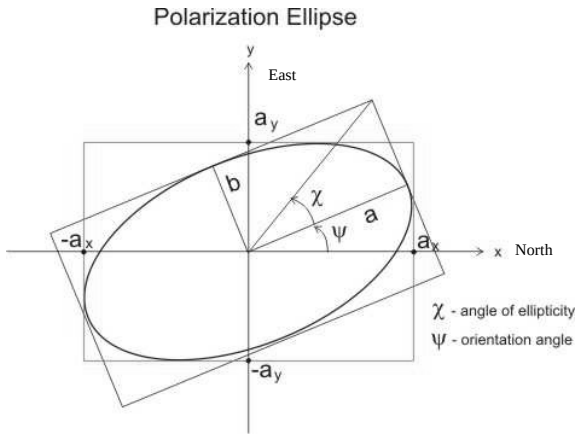

Figure 2.2: Description of the general state of polarization of an antenna in terms of the characteristics of an ellipse, drawn by the electric vector in the transmission of a sinusoidal signal. Ψ is the position angle of the ellipse, measured as an angle of the major axis with respect to the x axis (from North through East), which points toward the direction of north on the sky, and χ is an angle, determining the shape of the ellipse. A wave approaching from the sky is traveling toward the reader, in the direction of the positive z axis. If, from the position of observer, the vector rotates counterclockwise, such a wave is considered to have right-handed polarization. If the vector rotates clockwise, the circular polarization is called left-handed. (For the on-sky view, the picture should be rotated 90° counter-clockwise). Credit: http://physics.usask.ca

ponents, δ_{RL} is a phase difference between them, and angular brackets designate the average value. Note that for the ideal case of monochromatic radiation $I^2 = Q^2 + U^2 + V^2$, but for the real finite bandwidth case the radiation is not 100% polarized and the inequality $I^2 \geq Q^2 + U^2 + V^2$ holds. The Stokes parameters have the dimensions of flux density or intensity, and they propagate in the same manner as the electromagnetic field. They could be determined by a direct measurement, or derived from measured quantities at certain point of the radiation field. The relative strengths of the Stokes parameters determine the state of polarization at that point. The Stokes parameters are related to the degree of polarization in the following way:

$$
\begin{aligned}
m_{\rm L} &= \frac{\sqrt{Q^2+U^2}}{I} \,, \\
\Theta &= \frac{1}{2}\tan^{-1}\left(\frac{U}{Q}\right) \,, \qquad\qquad 0 \leq \Theta \leq \pi \,, \\
m_{\rm C} &= \frac{V}{I} \,, \\
m_{\rm tot} &= \frac{\sqrt{Q^2+U^2+V^2}}{I} \,,
\end{aligned}
\tag{2.19}
$$

where $m_{\rm L}$ is the degree and Θ is the positional angle of the plane of linear polarization, $m_{\rm C}$ is the degree of circular polarization, and $m_{\rm tot}$ is the total polarization degree. Q, U and V can be positive or negative, and I is strictly positive. In interferometry, the correlator output is related to a certain combination of the Stokes parameters of the incoming radiation at the corresponding spatial scale. Such Stokes parameters, measured by the two spaced antennas, are referred to as *Stokes visibilities*, and they represent the complex visibility for the distribution of the corresponding Stokes parameter over the source, not simply the intensity or brightness of the radiation. In the text below, in all formulas Q, U and V and I stand for the Stokes visibilities, unless otherwise is mentioned.

Radio telescopes measure the state of polarization of the incoming radiation in two different ways. Some antennas are equipped with perpendicular dipoles x' and y'. Each of those dipoles receives one component of the electromagnetic field, and the Stokes parameters can be easily calculated from the measured quantities. Such system is used, for example, at the Australia Telescope Compact Array (ATCA). The second type of receivers is equipped with two feeds sensitive to the two opposite circular polarizations, right and left, which are observed simultaneously and recorded separately. The Very Large Baseline Array (VLBA), which was used

to obtain data for this thesis, is an example of such radio telescope array. Consequently, in this and further sections I will present polarization observations theory, calibration and data reduction for the case of the circularly polarized feeds, with occasional comments on the differences with the linearly polarized feed systems like ATCA.

The output of the receiver, related to each circular component of polarization is normally marked as R or L, and in all calculations below I use this notation to define which polarization I am referring to. An antenna pair, thereby, provides four correlator outputs, which are related to the Stokes parameters as follows:

$$\begin{aligned} &< RR^* > \propto (I+V)/2\ , \\ &< RL^* > \propto (Q+iU)/2\ , \\ &< LR^* > \propto (Q-iU)/2\ , \\ &< LL^* > \propto (I-V)/2\ . \end{aligned} \tag{2.20}$$

The real antenna response to the incoming radiation, however, is influenced by the non-ideality of the receiving system. The observed circular polarization component contains errors due to the instrumental effects, which have to be calibrated out. The general approach to the description of the instrumental polarization errors is that the circularly polarized feed receives a certain amount of the opposite-handed polarization, e.g., the L feed receives a certain amount of R polarization, which is called *leakage*. The amount of leakage is denoted by D, and known as a *leakage term* or a *D-term*. One can write down registered voltages, considering the leakage:

$$v'_{\rm R} = v_{\rm R} + D_{\rm R} v_{\rm L}, \qquad v'_{\rm L} = v_{\rm L} + D_{\rm L} v_{\rm R}\ , \tag{2.21}$$

where v'_p is an observed voltage of the polarization p, v_p is a 'true' voltage, which would be observed with an ideal feed which has no leakage, and D_p is a leakage term for the corresponding polarization. For the contemporary interferometers the amount of leakage varies from 1 % to 10 %. For the VLBA antennas, values of D-terms are less than a few percent. Thus, for the correlator output (2.20) of the polarized signals from real antenna pairs in the case of weak polarization (for example, of the Active Galactic Nuclei), one can omit all terms containing the product of two D-terms or product of D-terms and Stokes visibilities as negligible

quantities. Finally, the real correlator output for the antennas m and n is:

$$\begin{aligned}
&< R_m R_n^* >' \propto (I+V)/2 \ , \\
&< R_m L_m^* >' \propto (D_m \mathrm{R} + D_n \mathrm{L}^*) I + (Q+iU)/2 \ , \\
&< L_m R_m^* >' \propto (D_m \mathrm{L} + D_n \mathrm{R}^*) I + (Q-iU)/2 \ , \\
&< L_m L_m^* >' \propto (I-V)/2 \ .
\end{aligned} \tag{2.22}$$

The *instrumental polarization calibration* procedure helps to determine the D-terms and apply them to the visibility data.

Calibration of polarization data

The polarization calibration is performed as a part of the AIPS *a-priori* calibration routine, except for the polarization position angle calibration. For this, one rather bright calibrator for the instrumental polarization and several *EVPA* (Electric Vector Position Angle, aka linear polarization position angle) calibrators should be included in the observation list.

During the observation, feeds of antennas on the alt-azimuth mount, like those of the VLBA array, rotate with respect to the sky. The removal of this effect is called *parallactic angle correction*. Parallactic angle is the angle between the great circle passing through an astronomical object and the zenith, and the hour circle of the object. During the polarization calibration, the parallactic angle of the object is calculated as a function of time for each antenna in the array for the whole observing session and applied to the data to remove the effect of the FOV rotation.

The cross-polarized (RL and LR) single-band delays and phase offsets between the basebands are removed from the data using fringe-fitting as another step in polarization calibration.

The final step of the *a-priori* polarization calibration is the instrumental polarization correction. For precise calibration, an unpolarized calibrator should be observed during the session for a sufficiently large range of parallactic angles at each station. However, for the circularly polarized feeds the algorithm is able to obtain D-term solutions for each antenna from just the parallel hand correlations $< RR^* >$ and $< LL^* >$ (2.22). For antennas with an alt-azimuth mount, observations of the calibrator, done with a sufficient time separation (and, therefore, difference of the parallactic angle) could be regarded as different calibrators due to the feed rotation. Also, there is no need to know the polarization state of the D-term calibrator before the observation. A total intensity model of the source

structure of a calibrator, which is built from the observed data, is enough to calculate the D-terms. These leakage term solutions are stable throughout the observing session.

After the instrumental polarization calibration, the imaging of the target sources is done, as described in the next section. The EVPA calibration is performed after all images of the total and polarized emission are reduced. To determine the linear polarization position angle, one needs external information about it at the epoch of observation at the same frequency. It is normally obtained from the calibrated observations with a single dish or a connected-element array. For these references one needs to include several sources in the observational schedule, for which polarization in the required radio frequency band is monitored by some other instrument, for example, by the Very Large Array (VLA) as a part of the 'VLA/VLBA Polarization Calibration Database' monitoring[1], as was done for Papers I and V. The observed EVPA of the calibrators is compared to one from the calibration monitoring, and a correction is applied to the target sources. AGN, which in most cases can serve as polarization calibrators due to their compactness, are often strongly variable sources. Sometimes, there is no calibrator monitoring data available sufficiently close in time to the target observation, then the EVPA must be interpolated for the date of the VLBI observation. It is recommended to observe several EVPA calibrators (minimum three) in order to average the resulting corrections and therefore mitigate interpolation errors.

2.3.4 Imaging

The limitation of spatial frequencies in u and v (the problem also known as 'sparse (u,v)-plane sampling', described in the next subsection) and the errors of measurement of the visibility function make imaging of VLBI data a non-trivial task. The mentioned above factors cause the emergence of artifacts on the source image, mostly periodic patches of 'ghost' emission or regions with negative flux. In contemporary VLBI this problem is overcome by using the *deconvolution - self-calibration loop*. Deconvolution uses a model of the source structure with simple components in order to deconvolve the real image from the point-spread function, and self-calibration corrects visibility data errors using the model visibilities.

[1] VLA/VLBA Polarization Calibration Database can be found online at `http://www.vla.nrao.edu/astro/calib/polar`

UV-plane coverage

For the exact restoration of the intensity distribution on the sky, one needs a full set of spatial frequencies, i.e. the complex visibility to be measured at every point (u,v). This case is called *full uv-plane coverage*, and the restoration of the image would simply be a mapping of the uv-plane into the image plane. This happens only when one considers a single aperture antenna as an interferometer. In practical radio interferometry, one has only a limited amount of spatial frequencies, which correspond to all the possible pairs of telescopes in the array, and their projection on the sky which are changing due to the Earth rotation during the observation. For example, the VLBA array has 10 antennas, therefore, there are 45 possible baseline combinations. When observations are done in so-called snapshot mode, the visibility function is defined only at the 45 points on the uv-plane. If observation the uses Earth rotation synthesis, each of those 45 points becomes a small arch (see Fig. 2.3). One can introduce a sampling function $S(u,v)$ which is zero at points where there is no information on the visibility function and unity at the points where it is defined. The main interferometry equation (2.11) has the following form:

$$I^D(l,m) = \iint V(u,v)S(u,v)e^{i\omega(ul+vm)/c}dudv\ . \tag{2.23}$$

where $I^D(l,m)$ is known as the *dirty image*. It is different from the *true brightness distribution* $I(l,m)$ because the sparsity of the (u,v)-plane coverage creates artifacts on the resulting source intensity map. Mathematically, the dirty image is a convolution of the true brightness distribution with the so called *dirty beam*, the point spread function of the interferometer:

$$B^D(l,m) = \iint S(u,v)e^{i\omega(ul+vm)/c}dudv\ , \tag{2.24}$$

The dirty beam has to be deconvolved from the data in order to obtain the true brightness distribution of the object.

Deconvolution

The dirty image (2.23) can be represented as a convolution of the true brightness distribution I with the dirty beam (2.24):

$$I^D = B^D \circledast I\ . \tag{2.25}$$

In order to deconvolve two functions, the Fourier transform is taken from expression 2.25:

$$\mathfrak{F}[I^D] = \mathfrak{F}[B^D(l,m) \circledast I(l,m)] = V(u,v) \cdot W(u,v) \ , \tag{2.26}$$

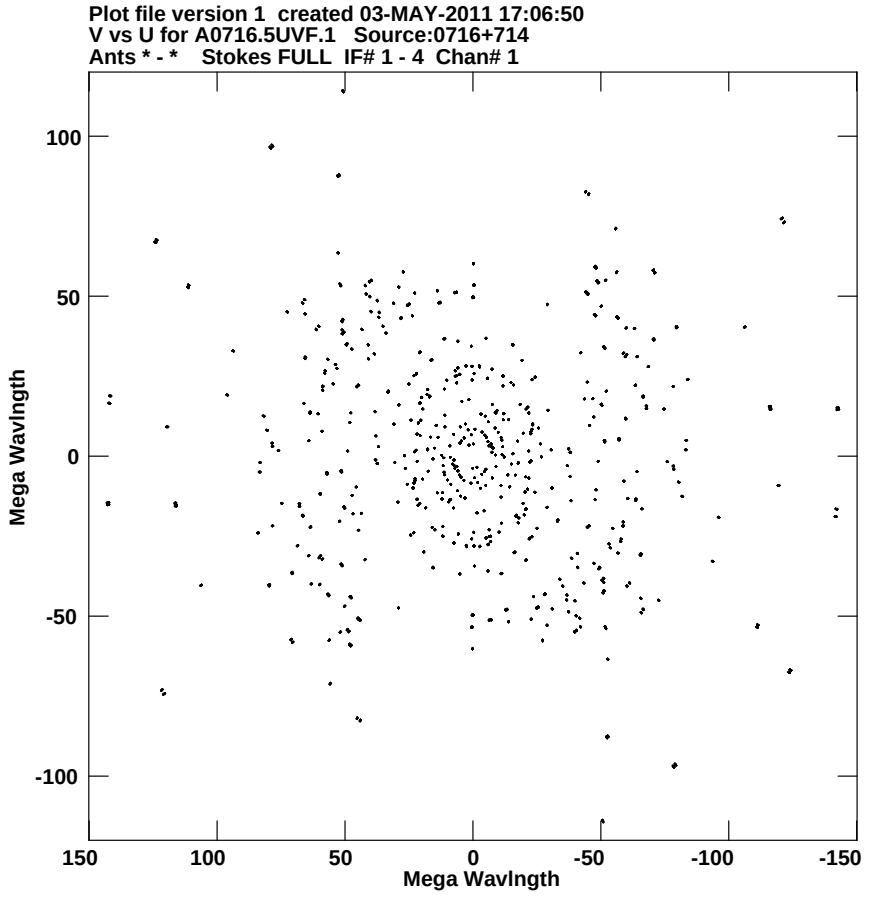

Figure 2.3: The (u,v)-plane coverage for the VLBI experiment BW072, epoch A, 5 GHz, program source blazar S5 0716+714. Total time of observation was nine hours, during which 10 scans five minutes long each were made of the program source.

where $\mathfrak{F}[f]$ defines the Fourier transform of function f, V is a true visibility function, and W is a transfer function, including weighting. Unfortunately, there are areas where the transfer function is equal to zero, so it is not possible to divide by it to obtain V. Therefore, in order to recover the true image from the observed visibilities, one has to replace the non-existing measurements with non-zero values. These non-zero values should be likely for the given true image, and should not add significant additional details to the image, i.e. be observable with the means of the array with the given transfer function. This imposes constraints on the emission: *positivity of intensity* and *spatial confinement*.

The most popular deconvolution algorithm is CLEAN, introduced by Högbom (1974). This is a convolution procedure in the (l,m)-plane. It models the source structure with a number of point sources, and then replaces each one of them with their convolution with the so-called *clean beam*, corresponding to the dirty beam without sidelobes. In practice, the clean beam is often chosen as a Gaussian with a half-amplitude width equal to that of the central lobe of the dirty beam.

The procedure of '*cleaning*', i.e. constructing the point-source model, is iterative. First, the so-called '*dirty map*' is constructed using the plain Fourier transform of the visibility and the weighted transfer function. Next, the algorithm finds an intensity peak i_p on this dirty map and places a point source with the intensity of some fraction of the peak γi_p. The response to this point source together with the sidelobe pattern is subtracted from the dirty map, and at the next iteration this residual map serves as a 'dirty map'. Iterations go on until the specified criterion is reached. The point sources added to the map on each iteration by the 'cleaning' procedure are called *clean components*, and γ is called a *loop gain factor*. Its value varies from 0.01 to 0.1 and it can be chosen by the data analyst. The criterion for interrupting the iteration process can be also chosen by the analyst, it is either emergence of the first/certain amount of clean component with negative intensity, obtaining certain number of clean components all together, or reaching the rms level by the peaks on the difference map. The resulting *clean component model*, the combination of all positive clean components, found in the iterative 'cleaning' - is then convolved with the clean beam, and then to this image the last residual map is added. The resulting map is an approximation of the true source image and called the *clean map*. One has to remember, though, that the errors of measurement are still present in the data, and they could be a source of noise or possible deviations from the true image.

Each clean component produces real and imaginary infinite sinusoidal patterns on the (u,v)-plane, filling the gaps between real observations. A realistic model of a resolved source may have in order of thousand clean components. If

the separation between clean components is smaller than the beam width, they represent the same region of the source.

Nowadays, there exists a large family of CLEAN algorithm variations. The three basic CLEAN methods, Högbom (Högbom, 1974), Clark (Clark, 1980) and MX (Schwab, 1984) are different only in the way of searching for the clean components, which allows to clean larger areas around the phase center. The more sophisticated algorithms, such as SDI (Steer, Dewdney & Ito, 1984) and Multi Resolution Clean (Wakker & Schwarz, 1988), use extended clean components instead of point-like ones and use more complicated searching strategies. These algorithms are mainly meant for recovering the structure of sources with high spatial dynamic range, where classic CLEAN may fail by creating image artifacts. CLEAN algorithms are implemented in all of the major packages for interferometry data reduction and/or imaging.

Apart from CLEAN, other types of deconvolution algorithms have been developed, however, they are less popular by far, even though some of them are implemented in common data processing software. The Maximum Entropy Method and its modification make up another class of deconvolution algorithms. The MEM method was first proposed by Frieden (1972), and considered for the use in radio astronomy by Ponsonby (1973) and Ables (1974). The idea of the Maximum Entropy Method is that the resulting map agrees with the measured visibility within the noise level and maximizes an *entropy functional*. It constrains the choice of visibility values in the areas on $(u,v)-$plane where measurements of visibilities are missing, in such a way that they minimizes introduced artifacts on the map. The entropy functional is defined slightly differently for different realizations of the MEM method.

For the general comparison of CLEAN- and MEM-based methods one can refer to the book Thompson, Moran & Swenson (2004), Chapter 11.3, and references therein. Also, in Paper III, the authors discuss in detail the MEM algorithm implementation in the AIPS data reduction package (see Cornwell & Evans, 1985) and the Generalized MEM algorithm introduced by Baikova (2007), and compare the results of the last one with the conventional CLEAN implementation as applied to kinematic studies of AGN.

There exist other deconvolution methods, which are based on different source removal and optimization algorithms, for example, MEM-based methods, Linear Minimum Mean Square Error (LMMSE), Non Negative Linear Least Squares (NNLS) and Compressed Sensing (CS). However, these methods are not yet well developed and hardly used in practice. For a review of the existing and new deconvolution methods one can consult Levanda & Leshem (2010).

Note that the deconvolution methods are highly non-linear, which alters the noise statistics of the resulting image.

Self-calibration

While the influence of the sparse (u,v)-plane sampling can be mitigated by using deconvolution, there are still residual amplitude and phase errors in the visibility data which lower the quality of the image. The data processing technique called *self-calibration* is used to determine antenna complex gains g_m and g_n by minimizing the square of the absolute value of the difference between the observed visibility and the model one. For an antenna pair *m* - *n*, the minimized expression will look as follows:

$$\sum_{\text{time}} \sum_{\substack{m,n \\ m<n}} w_{mn} |V_{mn}^{\text{obs}} - g_m g_n^* V_{mn}^{\text{model}}|^2 \,, \tag{2.27}$$

where all the quantities are functions of time. Self-calibration could be *phase only*, when only phases of the complex gains are corrected, and *amplitude and phase*, when amplitudes and phases of the gain factors are solved for together.

Self-calibration is applied in combination with deconvolution. First, deconvolution provides a model that is used for self-calibration to find the gain factors. On the next step, the found gains are applied to the data, and the modified visibilities are Fourier-transformed to obtain the new dirty image. Then, a new model is deconvolved from the dirty image, and the cycle repeats again. Phase self-calibrations are applied first to the raw data, and only when a good source model is achieved, amplitude calibration can be performed. For the VLBI data it is common to perform the first phase calibration with the point-source model and a *solution time interval* equal to the averaging time. All consecutive phase calibrations are performed with the model provided by the deconvolution algorithm. After the major phase errors are corrected, the first long-interval amplitude and phase self-calibration is performed. The solution interval of the amplitude and phase self-calibrations consecutively decreases from the observation time to the averaging time, and they are alternated with the phase self-calibrations at the shortest time scales. This scheme helps to decrease the residual errors cycle after cycle. It should be noted that the self-calibrations can only improve antenna-based errors and has no influence on the baseline-based ones.

Closure quantities

Even if not self-calibrated, phases and amplitudes constrain the model of a source structure. Following equation (2.17) for visibility, a sum of the phases of any three baselines, also known as *closure triangle*, does not depend on the antenna-based errors. The observed phase for the baseline $i-j$ has the following form:

$$\theta_{ij}^{\rm obs} = \theta_{ij}^{\rm true} + \phi_i - \phi_j \ , \tag{2.28}$$

where $\theta^{\rm true}$ is a true baseline phase, ϕ are the station-based errors. The additive errors ϕ cancel each other, so the *closure phase* consists only of the sum of true visibility phases:

$$\Phi_{mnp} = \theta_{mn}^{\rm obs} + \theta_{np}^{\rm obs} + \theta_{mp}^{\rm obs} = \theta_{mn}^{\rm true} + \theta_{np}^{\rm true} + \theta_{mp}^{\rm true}. \tag{2.29}$$

A closure relationship also exists for the amplitude of the visibility function. The amplitude closes on the baseline quadrilateral. One can write down the observed visibility amplitude for the baseline $i-j$:

$$A_{ij}^{\rm obs} = g_i g_j A_{ij}^{\rm true} \ ,$$

where g is the gain factor of each antenna and $A^{\rm true}$ is the true amplitude. A combination of amplitudes of the antennas m,n,p and q at the vertexes of the closure quadrilateral, also called the *closure amplitude*, has the following form:

$$\Gamma_{mnpq} = \frac{A_{mn}^{\rm obs} A_{pq}^{\rm obs}}{A_{np}^{\rm obs} A_{mq}^{\rm obs}} = \frac{A_{mn}^{\rm true} A_{pq}^{\rm true}}{A_{np}^{\rm true} A_{mq}^{\rm true}} \ . \tag{2.30}$$

Note that the baseline-based errors are not closing.

Closure equations limit the number of independent variables, while solving for the complex gains in a self-calibration process. Self-calibration does not affect closure quantities, so they can provide additional information about the source structure. Even though the closure relations can not be used directly for imaging, they are vital for testing the source model quality. They can also be used in order to distinguish between two different models of the same source and to find which one of those reproduce the data better. Such a comparison of two models was performed in Savolainen et al. (2002), where closure phases on the longest baselines were used to find a partially resolved component of the AGN jet, which was located less than one beamwidth away from the VLBI core. Authors of this paper model fitted the data with two different models, one of which had only one com-

ponent (core model), and the other model contained two components (core+jet model). After that the authors compares how well each of the models reproduced the closure phases at long baselines, and found that the core+jet model provided much better fit.

2.3.5 Model fitting

In many cases, the source structure should be parametrized for quantitative analysis, for example to examine structural changes with time, estimate a physical size of the object or relative position of its parts, or classify the source based on the type of structure. The standard approach is to decompose the map to a number of simple components, for example point sources, or circular/elliptical sources with a Gaussian distribution of flux. Choice of positions and sizes of the model component is done based on the visual inspection of the map. From this point, there are two alternative approaches: model fitting in the *visibility domain* and in the *image plane*. The first method is more powerful and accurate, also it is easier to estimate errors of the model-fitting and discard the wrong model by visual comparison of the model and observed visibility. The second approach is weaker in many respects, because the image can contain deconvolution errors, and the noise statistics are influenced by the non-linear deconvolution procedure. However, image-plane model fitting is easier to implement, and computationally it is more efficient. Both approaches are realized in contemporary data reduction packages, however, the visibility model fitting is definitely more popular.

The data for Paper I were model fitted in the visibility space using the Brandeis University package VISFIT (the main idea of the algorithm used in VISFIT and an example of its use can be found in Roberts, Gabuzda & Wardle, 1987, recently the package was modified and updated by V. Bezrukovs and D. Gabuzda from University College Cork, Ireland). For Paper III, a model fit for the conventional method was performed using Difmap package (Shepherd, Pearson & Taylor, 1994), which fits directly to the real and imaginary parts of the observed visibilities using the Levenberg-Marquardt non-linear least squares minimization technique. For the GMEM data the model fitting was done in the image plane.

2.3.6 Circular polarization imaging

Some mechanisms of radiation generation, for example synchrotron emission, may produce circularly polarized radiation. Also, the Faraday conversion creates circular polarization from the linear one when it passes through plasma. The

circular polarization in AGN from single dish radio observations is reported to be in order of several tenth of a percent (e. g. Rayner, Norris & Sault, 2000; Cenacchi et al., 2009; Agudo et al., 2010).

As it was mentioned in section 2.3.3, the instrumental polarization may be the limiting factor for the observation of weakly polarized sources. However, the standard D-term calibration is proven to be precise enough for circular polarization imaging. Already Homan & Wardle (1999) report, that for the VLBA array, with its values of D-terms of about 1 % - 5 %, and using the standard instrumental polarization calibration procedure, the D-term calibration errors were not larger than 15 %. These errors caused noise on the circularly polarized images of about 0.2 % of the corresponding linear polarization. Therefore, the main source of noise on the circular polarization map is errors in the determination of complex gains. Therefore they should be determined with good accuracy.

The self-calibration loop (see section 2.3.4), in the standard case, is performed under the assumption that the circular polarization $V = 0$, which is realized by minimizing two functionals (see 2.27) for each antenna pair *m* and *n*:

$$\begin{aligned} &|< R_m R_n^* >^{\mathrm{obs}} - g_m g_n^* I_{mn}^{\mathrm{model}}| \text{ and} \\ &|< L_m L_n^* >^{\mathrm{obs}} - g_m g_n^* I_{mn}^{\mathrm{model}}| , \end{aligned} \tag{2.31}$$

which obviously makes an assumption about zero intrinsic circular polarization of the observed radiation. It is possible to perform the self-calibration in a different way, so that the functional is minimized with respect to both *RR* and *LL* visibilities at the same time:

$$|\frac{(< R_m R_n^* >^{\mathrm{obs}} + < L_m L_n^* >)^{\mathrm{obs}}}{2} - g_m g_n^* I_{mn}^{\mathrm{model}}| . \tag{2.32}$$

In this way, there is no assumption made about the circular polarization value. However, only the average of *R* and *L* for each antenna is calibrated in this case, and relative gain ratio for opposite senses of polarization, g_R/g_L, remains uncalibrated. In order to set the correct right to left gain ratio, one has to to make sure that the incoming circular polarization is genuinely zero, which can be done by adding to the observing program a known circularly unpolarized source as a calibrator. The complex gains for each antenna can be determined using calibrator data by applying one round of self-calibration, which considers *RR* and *LL* separately (see equation 2.31), and the solutions are then transferred to the whole data set. Taking into account the time variability of gains, the observing session should be planned so that the unpolarized calibrator is observed between the tar-

get sources several times during the session. This method of circular polarization calibration is called *gain transfer*. The gain transfer method was developed and first implemented by Homan & Wardle (1999). If there are no known circularly unpolarized sources which are bright enough to be used as calibrators, but there are many objects observed within the same observational session, one can use them all (except for those with known high circular polarization) in order to construct a calibration *gain curve*. In this case, each of the sources with weak circular polarization is treated as a calibrator (described above), however, the solutions are not applied to the data right away, but instead are merged into one solution table, which is then smoothed. It is possible, under assumption that circular polarization is distributed randomly, that for a large amount of calibrators there is equal amount of sources with positive and negative signs of circular polarization. In the merged gain table, those sources cancel each other, and the final solution is equivalent to that of the unpolarized calibrators. For the smoothing time intervals of more than four hours and less than 24 hours, the result does not strongly depend either on the parameter value or on the smoothing function, as reported by Homan & Wardle (1999).

After transferring the calibrator or combined gain curve to the data set, the stokes V visibility is edited and then imaged in a standard way with the use of the AIPS task *IMAGR*, in which the CLEAN algorithm is implemented.

It is necessary to mention, that antenna arrays such as ATCA, in which antennas are equipped with linearly polarized crossed-dipoles feeds, are much better suited for imaging the circular polarization, for the following reason. In such arrays, the measured circular polarization is proportional to the difference of the two cross-handed correlations $< XY^* >$ and $< YX^* >$ on each baseline, and errors of the antenna gains lead to the leakage of the Stokes parameters Q and U into the V. As opposed to linearly polarized crossed-dipoles feed systems, in circularly polarized feed systems, the measured circular polarization of the incoming radiation is proportional to the difference of the two parallel-handed correlations $< LL^* >$ and $< RR^* >$, and, therefore, the Stokes parameter I is leaking into the V. Since the Stokes parameters Q and U are smaller in magnitude than I, the errors of the measured circular polarization are smaller than those obtained with circularly polarized feed systems like VLBA. Thus, for the linearly polarized feed design, the determination of the leakage terms (D-terms) is more critical for the circular polarization calibration than determination of the antenna gains, besides leakage terms, unlike gains, are rather stable and easy to determine (see Rayner, Norris & Sault, 2000, for the details of ATCA circular polarization observations and calibration).

Chapter 3

Active Galactic Nuclei

Active galactic nuclei (AGN) are the most luminous extragalactic objects. They lie in the centers of massive galaxies, and their non-thermal emission outshines all the thermal radiation from the stars and gas of the host galaxy. In this chapter, I give a short overview of the discovery and history of the radio observations of AGN, touch the classifications of different AGN types and their unification scheme, and give an outline of the generally accepted model of the AGN driving engine.

3.1 An introduction to AGN and important milestones.

3.1.1 Seyfert galaxies

AGN is a very broad class of objects with many subtypes. In the first years of AGN studies, new classes of objects were emerging with the increase of the observed sample. Even though some of the AGN have been observed since the 19^{th} century without realizing their nature. For example, historical optical light curve of the AGN OJ287 dates back to 1890 (e.g., Sillanpää et al., 1988), and for BL Lac – to 1896 (Fan et al., 1998). These objects were thought to be variable stars. The real history of AGN starts with Seyfert's observations of bright emission lines in the "nuclei of spiral nebulae" in 1943 (Seyfert, 1943), which lead to a discovery of a new class of galaxies with a bright core: *Seyfert galaxies*. Later the classification was updated, and Type 1 and 2 of the Seyfert galaxies were introduced. The spectrum of a Seyfert type 1 is characterized by broad emission lines and the presence of forbidden lines, and type 2 has only narrow emission lines. Also the fractional types (e.g., Seyfert 1.5, 1.8, etc) are used, depending on the relative strength of the narrow and broad lines.

3.1.2 Quasars

In the 1950-60s, numerous new sources were observed in the radio domain with no optical counterpart. The third Cambridge Cataloque of Radio Sources (3C) at frequency 158 MHz was published in 1959 (Edge et al., 1959), and a revised version (3CR) - at 178 MHz in 1962 (Bennett, 1962). They contained several hundreds of point-like sources, unidentified in the optical domain, for the observers from around the world to try finding the optical counterparts. Indeed, in 1960, the source 3C48 was cross-identified with a faint blue starlike object which had broad emission lines, but the nature of this source remained unclear until 1962, when the optical counterpart of 3C273 was found with the method of Lunar occultations (Hazard, Mackey & Shimmins, 1963). The spectrum of the 13th magnitude star-like source contained emission lines, which were identified as the Balmer-series lines of hydrogen and MgII λ2798 line that were red-shifted by 16 %, which corresponds to z=0.158 (Schmidt, 1963). Soon after that, redshifts of 3C48 and other sources from this catalog were identified, and the term 'quasar', derivative of the 'quasi-stellar radio source', was coined in 1964. In the year 1965 it was discovered that they are highly variable, and variability timescales suggested exceptionally small sizes (Sholomitskii, 1965a, English translation of this article is Sholomitskii, 1965b; Dent, 1965).

Quasars are the most luminous of all AGNs: their total luminosities go up to $10^{13} L_{\odot}$. The redshifts at which they have been observed range from z $\sim$ 0.1 to 7.085 (the most distant quasar known so far is ULAS J1120+0641, Mortlock et al. (2011)). Quasars are found at distances up to 13 billion light years away from us, which make them one of the most distant object types observed, alongside with the radio galaxies and gamma-ray bursts (GRB). Quasars are spectroscopically similar to the Seyfert type 1 galaxies, as broad emission lines with widths up to $10^4 km/s$ are present in both classes.

3.1.3 Power source and the AGN central engine

The *Activity* of the nucleus is a complex phenomenon which makes AGN different from any of the 'normal', quiescent galaxies. AGN are the most luminous sources. They are variable on rather short time scales throughout the whole electromagnetic spectrum (e.g., Wagner & Witzel, 1995), and the variability of AGN was discovered soon after the discovery of the 'quasi-stellar radio sources' themselves (see, e.g., the review by Kellermann & Pauliny-Toth, 1968). Some variations happen on the scales of less than a year, which implies that the radiating region within the

source is less than one light year across. The search for a suitable power source (also known as *the central engine*) for such an object started in 1950s by A. Ambartsumian, who first raised the issue of the activity of the galactic nuclei and proposed that they must contain bodies of enormous mass and unknown nature (Ambartsumian, 1958). With time, many different hypotheses were produced, including very exotic ones. However, the most viable hypothesis utilized accretion of matter onto a supermassive black hole (SMBH, $M \gtrsim 10^6 M_\odot$) in the center of a galaxy. Nowadays, this is the generally accepted model for the AGN power source.

It is now generally agreed that all galaxies have a SMBH in the center, however only some of them become active, i.e. start to accrete matter from their neighborhood (see a comprehensive review of the recent advances in the field of study of SMBHs in centers of normal galaxies by Ferrarese & Ford, 2005). It happens in galaxies of spiral or elliptical type, and in the presence of an active nucleus the galaxy is called the *host galaxy* of the AGN. The activity process causes a plethora of observed phenomena, that characterize AGN.

The gas which is attracted to the central parsec of the galaxy forms clouds that are rotating around the SMBH, colliding and losing their kinetic energy. As they reach the close vicinity of the black hole, the clouds disintegrate and the matter forms a rotating disc. In the accretion disc, the matter is losing its angular momentum due to viscosity or magnetic drag, and, thereby, the gas is transferred inside the last stable circular orbit around the black hole, where from it falls via spiral trajectories below the event horizon, *feeding* the SMBH.

The accretion disk emits thermal radiation, and hot gas in the clouds, rotating around the center at a broad range of distances, emits radiation in spectral lines. The velocity of the clouds depends on their distance from the center, and the width of the emission lines depends on the velocity of the emitting gas. There are two different regions in the AGN which can be spectroscopically distinguished: the broad line region (BLR), which is composed of dense gas clouds ($n_e > 10^9 cm^{-3}$) at the distance of less than 1 pc from the SMBH and rotating with the speeds of of 1 000 - 25 000 km/s, and the narrow line region (NLR), consisting of low density ($n_e \approx 10^3 cm^{-3}$) clouds rotating around the central SMBH with the speeds of $<$ 500 km/s (Peterson, 2006). In a number of AGN, there is also present a thick obscuring torus of cold dust around the accretion disc and the BLR, and a corona of hot electrons around the whole central engine.

In some cases the accreting SMBH causes an outflow of matter perpendicular to the plane of the accretion disk, which is called the *jet*. The plasma in the accretion disc is interweaved with the magnetic field. Rotating, the accretion disc

twists the magnetic field lines, creating a helical magnetic field in the jet. The charged particles wind around the magnetic field lines in the jet and emit non-thermal synchrotron radiation in the broad range of energies (from radio up to TeV).

A schematic view of the current model of the AGN central engine is presented in Fig. 3.1.

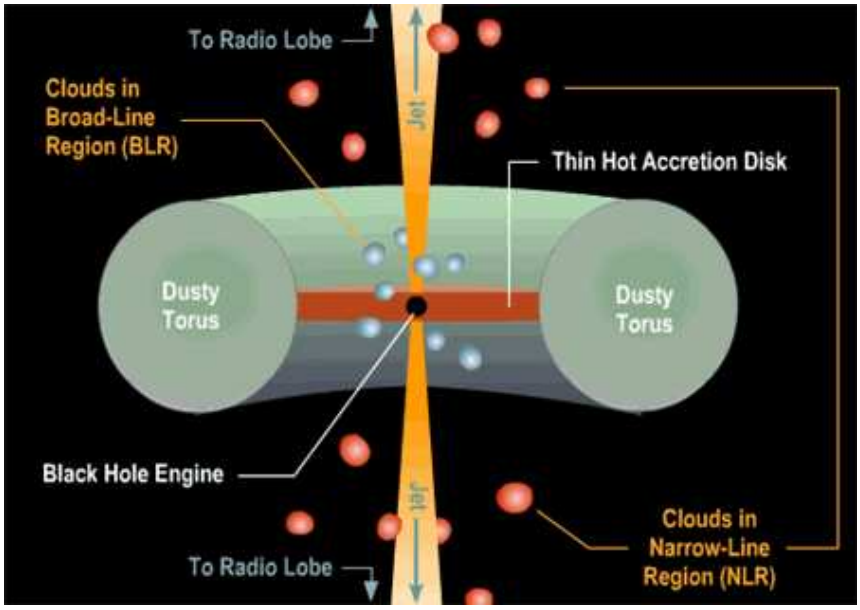

Figure 3.1: Schematic view of the AGN central engine model. Credit: Brooks/Cole Thomson Learning.

3.2 Classifications of AGN

In this section, I will briefly describe different classifications which are applied to AGN. They are all based on the observed properties of the sources and do not take into account the physics of the central engine. They are, also, often confusing since they reflect the history of the discovery and observations of different AGN types rather than real physical differences between them.

Morphological classification is the most basic type. With connected-element interferometry and VLBI it is possible to map the structure of the radio sources at

a broad range of spatial scales. The most coarse division based on the observed characteristics can be made between the *core-dominated* radio sources, whose compact core is brighter than the extended component, and the *lobe-dominated* ones, which have two bright *lobes* - regions of extended emission, located symmetrically at both sides of the core. The lobes extend far beyond the host galaxy of the source, up to several megaparsecs, and their brightness is much higher than that of the core.

The lobe-dominated sources have clear flux-dependent properties, which were discovered by Fanaroff & Riley (1974) during their studies of the sources from the 3CR catalog. They found that the lobe-dominated AGN can be divided into two major classes: the sources of the Fanaroff-Riley I (FRI) class have a flux at 178 MHz below 5×10^{25} watts and have a distinct steep-spectrum radio lobes, which are connected to the bright central source with a smooth continuous double-side radio jet. The outer edges of the lobes are fainter than the ones which are closer to the core. The Fanaroff-Riley II (FRII) sources are more luminous at 178 MHz, and their lobes are edge brightened, i.e. the outer edge of the lobe is brigher than the inner one. There are distinct 'hot spots' visible at the outer-most parts of the lobes. Jets of the FRII sources are not so smooth as in the FRI sources, and, in many sources, only a one-sided jet is visible (the second lobe is not connected to the core on the image).

There is a common term for those active galaxies that emit bright synchrotron radiation from their cores and radio lobes at the radio frequencies - *radio galaxies*. Since the lobes emit a vast amount of energy by the synchrotron process, they must contain relativistic electrons and a magnetic field and have a source of energy to compensate for the radiative and expansion losses. The jet must be the medium that transfers the energy from the central engine to the lobes, and this is the argument for the existence of the jet even in the FRII sources with extremely bright lobes which are outshining the jet completely.

Spectral classification is applied to quasars, as they were first found with single-dish observations. The whole source fits inside the main beam of a telescope. Therefore, it seemed to be point-like and morphology could not be used as a ground for classification. *Radio-loud* quasars are those whose flux in radio is higher than the optical one, the rest of quasars are called *radio-quiet* or radio-weak. Approximately 10 % of all quasars are radio-loud. This class is divided further according to its radio spectrum to the *steep-spectrum* lobe-dominated and the *flat-spectrum* core-dominated radio quasars (FSRQs). FSRQs are rapidly variable and have high polarization. If resolved in the radio domain, they are dominated by a compact radio core. The structure of FSRQs resembles that of the FRII class

objects, though the jet in FSRQs is brighter than in the ”classic” FRII sources.

BL Lac objects is another class of AGN with specific properties. This source type is named after the prototypical source BL Lac (quasar B2200+420). BL Lac objects have a rather compact radio structure, resembling that of the classic FRI type sources, though there are no lobes in most of BL Lac objects. Their line spectrum is almost featureless, emission lines are either absent or very weak (the boundary for the FWHM of the lines was set to 5Å, however, this value is based solely on the observations and does not represent any internal physical property of the source). The distinct structural feature of the BL Lac objects in the radio domain is the *one-sidedness of the jet*. These sources are violently variable on different time scales and at all observed wavelengths.

BL Lac objects together with the FSRQs compose a compound class of AGN called *blazars*. These two subclasses are not physically similar: the intrinsic luminosity of FSRQs is higher, and they have, on average, more powerful jets. However, they represent the same phenomenon - *relativistic beaming* of the radiation. This phenomenon will be explained in more detail in section 4.2.1.

Radio-loud quasars are sometimes also classified based on their *optical polarization*: if the polarization degree is < 3 %, the quasar is called *low polarization*, whereas a *high polarization* quasar is a quasar with a degree of polarization > 3 %.

BL Lac objects together with radio-loud quasars and radio galaxies make up a class of *radio loud AGN*.

3.3 Unification model

The confusing classification discussed in the previous section only helps to systematize the previously obtained knowledge of the AGN observational properties rather than helps to understand the general picture of the AGN phenomenon, and to learn what physical reasons cause differences and similarities between AGN types. In order to reconstruct the whole picture one has to be able to explain the variety of observational phenomena related to the AGN using simple theoretical ideas that is consistent with the observed data.

As it was mentioned earlier (section 3.1.3), the generally accepted theoretical model of AGN states that there is a supermassive black hole in the center of the galaxy, which attracts matter to the center with its gravity and consumes it via disc accretion. The *unification model* (or *unified scheme*) attempts to explain differences between AGN classes by changes of only a small number of its parameters, preferably just one. Since the AGN obviously emits a part of its radiation

anisotropically, the logical parameter for such a distinction could be connected with the orientation of the object with respect to the observer, for example, *angle of the jet to the line of sight*. The unification scheme is based on a broad range of spectral observations of the AGN, a comprehensive discussion of its observational prerequisites can be found, for example, in the paper Antonucci (1993) or Urry & Padovani (1995), and short and less detailed explanation of the unification idea can be found in Peterson & Wilkes (2000).

The orientation-based unification scheme is applied to the radio-loud and radio-quiet sources separately. As it was mentioned before (section 3.1), the main difference between radio-quiet Seyfert galaxies of type 1 and type 2 is that the type 1 exhibit broad emission lines (FWHM $\approx 10^4 km/s$), and type 2 do not. In the unification model this distinction is explained by the fact that the obscuring molecular torus, surrounding the central engine, blocks the light from the BLR in the Seyfert 2 galaxies since they are observed more 'edge-on', whereas in the Seyfert 1s, that are seen more 'face-on', it freely reaches the observer. The light from the NLR, which is further away from the center, is not blocked by the torus.

Radio galaxies and blazars belong to the group of radio-loud AGN. If the radio-loud object is observed more or less 'edge-on' (at some moderate angle to the jet), the observer sees an ordinary radio galaxy of the type FRI or FRII. As the viewing angle of the jet decreases, relativistic beaming starts to play a role. The relativistic effects enhance the observed flux density, increase the apparent speed of the jet, blue-shift the spectrm and shorten the observed variability timescale (see section 4.2.1). An FRI type source, viewed 'jet-on', becomes a BL Lac, and a FRII type radio galaxy becomes a flat-spectrum radio quasar. In other words, a radio galaxy viewed jet-on becomes a blazar. The FRI / FRII types are different in luminosity, therefore, the reason for distinction of those two types could be attributed to the mass of the SMBH and/or the mass accretion rate.

An attempt to unify radio-loud AGN with radio-quiet ones is called *grand unification*. High-resolution observations shown that the main structural difference between those two types of AGN is that the radio-loud sources have a jet, consisting of synchrotron-emitting plasma, while the radio-quiet sources do not. The reason for this discrimination is attributed to the SMBH mass and spin and rate of accretion; properties of the host galaxies, their environment and neighborhood, and evolution of the source are mentioned as secondary causes. (e.g. Meier, 2002; Lacy, 2003). However, there is no complete theory for grand unification at the moment.

All sources which are considered in the papers composing this thesis belong to the blazar type. As it is clear from this chapter, they are radio-loud AGN viewed

'jet-on'. At the milliarcsecond scale the jet appears one-sided due to the relativistic beaming, with superluminal apparent motion observed in it. Therefore, the AGN jet theory in the next chapter will be given as applied to blazars, and details concerning other classes of AGN will be specially mentioned.

Chapter 4

Compact jets

4.1 Jets in nature

Outflows and inflows of matter are present in all types of AGN including the radio-quiet ones, but the compact collimated jets as distinct structural elements are present only in radio-loud sources. Jets are observed in the optical and radio bands, and they look as narrow bright streams connecting a radiogalaxy to its lobes, or as simple linear outflows from the center of galaxy. Jets are also observed in galactic objects - young stellar objects (YSOs) and binary systems (*microquasars*), although physics of the YSO jets is different from that of the jets in AGN or microquasars. However, the nature of all jets is the same: a jet is a visible manifestation of anisotropic mass ejection from an astronomical object. Microquasars are galactic objects, they are X-ray binaries that contain a stellar mass black hole and a normal star at a late stage of evolution, when the gas from the star is accreted on the black hole. The name 'microquasars' comes from the similarity of physical processes in these objects with those in AGN. The central engine in such binary systems closely resembles that in AGN: a black hole, accretion disc and collimated jet. These two types of objects are analogous to each other, the difference is in the emitted power and time scale of processes in these systems: they are scaled down together with the black hole mass (Heinz & Sunyaev, 2003). Observed properties of the microquasar jets resemble those of FRI objects (Spencer, 2005). Studies of microquasars contribute to the understanding of AGN physics. There is evidence that microquasars also take their place in the grand unification scheme (Merloni, Heinz & Di Matteo, 2005). The book 'The Jet Paradigm: From Microquasars to Quasars,' T. Belloni (2010), addresses similarities and differences between jets in those two types of objects.

4.2 Apparent structure and kinematics

On an aperture synthesis map (arcsecond scale), the jet of an FRI source looks like a bright smooth continuous stream, whereas jet of an FRII source looks fainter and more 'clumpy'. On VLBI images (milliarcsecond scale), the one-sided jets of blazars have a steep spectrum, at higher frequencies, the emission of an extended jet fades away very quickly. Some blazars have relatively long, clumpy and wiggling jets (e.g., OJ287, 3C279), some have short and smooth jets, dimming to the edge (e.g., S5 0716+714, 2131-021), some sources are compact and core-dominated with jets emerging only at certain epochs (e.g., B0420-014, J1749+096).

The central engine of an AGN is not directly visible on VLBI maps. The brightening that is normally observed at the beginning of the jet, referred to as the VLBI core or a *pseudo-core*, is, in fact, the optically thick inner part of the jet, closest to the SMBH. Apparent brightness enhancements, 'clumps', which are frequently observed in the jet, are called *knots* or *(jet) components*. Series of subsequent high resolution observations of an AGN, performed with the time intervals on the order of several weeks or months, are used to study how the structure of the jet changes with time. In most cases, components move along the jet in the outward direction, from the VLBI core towards the optically thin part, however, in some sources, retrograde motion is observed. Alongside with the moving components, some jets contain also the *stationary* ones. Stationary component do not change their position with respect to the VLBI core. Some stationary features were observed by different authors in several different projects, with time separation between observations on the order of several years. These observations prove a good time stability of the stationary features. Jorstad et al. (2001) concludes, that the stationary components are not the same type of components as the moving ones, but with velocity equals to zero. On the contrary, they have different nature. A discussion of the jet components and their physical meaning can be found in section 4.5.3.

4.2.1 Blazar phenomenon and relativistic beaming

As it was mentioned before, blazars form a compound class of AGN that unites the FSRQs and the BL Lac objects. Observational properties of those two subclasses can be explained if their jets are closely aligned with the line of sight of the observer. Provided that, the effect of *relativistic beaming*, also known as the *Doppler beaming*, can take place. The hypothesis of beaming in compact radio sources was

first suggested by M. Rees in 1966 (Rees, 1966), and observational evidences for it were found later: superluminal motion in 3C 279 and 3C 273 were already observed in early VLBI experiments at the Goldstone-Haystack two-element radio interferometer (Whitney et al., 1971; Cohen et al., 1971). A very useful consideration of the special theory of relativity as applied to the jets physics can be found in Ghisellini (1999). Let us assume the following parameters of the jet: bulk plasma velocity in units of the speed of light is $\beta = v/c$, where v is measured in the reference frame of the source, angle of the jet to the line of sight is θ. The spectrum of radio emission from the source has exponential form $S_\nu \propto \nu^\alpha$, where α is the *spectral index*. The corresponding Lorentz factor of the jet in this case is:

$$\gamma = (1-\beta^2)^{-1/2} , \tag{4.1}$$

and the kinematic *Doppler factor* (which is sometimes called the *beaming factor*) is

$$\delta = \frac{1}{\gamma(1-\beta\cos\theta)} . \tag{4.2}$$

In the subsequent equations primed quantities are measured in the source reference frame, and unprimed quantities are measured in the reference frame of the observer. The effect of beaming leads to the scaling of the observed flux density:

$$S_\nu = \delta^{x+\alpha} S'_\nu , \tag{4.3}$$

where $x = 2$ for a smooth continuous flow and $x = 3$ for an isolated optically thin emitting source (e.g., Cohen et al., 2007). It happens because radiation from a relativistically moving source is beamed into a cone with opening angle of $\sim 2/\gamma$ that is oriented towards the direction of motion with its axis parallel to the velocity vector. At the same time, the frequency of radiation also increases:

$$\nu = \delta\nu' . \tag{4.4}$$

The time scale of photon arrival would also change due to the relativistic effects:

$$\Delta t = \delta^{-1}\Delta t' , \tag{4.5}$$

which makes apparent variability to be faster than the internal one. Due to the beaming effect, the brightness of the jet that is moving towards the observer is enhanced, and the opposite jet, pointing away from the observer, is dimmed. As a

result, an apparent ratio of the fluxes of two initially equally bright jet components can be as high as 10^3. The dynamical range of VLBI maps is usually lower than that, and only the 'front' bright component of the jet would appear on an image. This is the reason why blazars demonstrate one-sided jets. If relativistic motion occurs at a small angle to the line of sight, and the velocity of plasma exceeds $\beta > 1/\sqrt{2}c$, then the apparent velocity of the jet measured by the observer on the sky plane may exceed c, in some cases significantly (in blazars, β is up to $50c$, the maximum of the distribution is at $\sim 10c$) (Lister et al., 2009; Piner et al., 2006; Jorstad et al., 2005):

$$\beta_{\rm app} = \frac{\beta \sin\theta}{1-\beta\cos\theta} \, . \tag{4.6}$$

Understanding the connection between internal processes in AGN and the observed parameters of their jets is vital since it gives a tool for deriving the physical parameters of a jet and AGN central engine from the VLBI data. This connection has been demonstrated in a number of publications. For example, the derivation of kinematic parameters for a conical relativistic jet could be found in (Gopal-Krishna et al., 2007), and analytical kinematic diagrams, showing the interdependence of jet parameters, are published in (Gopal-Krishna, Sircar & Dhurde, 2007).

4.3 Polarization of emission from AGN jets

Emission from jets is linearly polarized. As soon as the principles of polarization interferometric observations (with a connected-element interferometer) were developed in the 1960s, the first linear polarization (LP) distribution measurements of AGN jets were made (Conway & Kronberg, 1969). The first successful VLBI polarization observations were carried out in the early 1980s (Cotton et al., 1984). A general discussion of calibration and imaging of the polarized emission with VLBI is given in Cotton (1993). Some extended features of blazar jets are reported to have polarization of up to 50 % (Lister, 2001; Lister & Homan, 2005), and LP in VLBI cores of blazars is on the order of a few percent. In some blazars, circular polarization (CP) is observed. In the majority of cases it is concentrated in the VLBI core, with the values on the order of tenths of percent (e.g., Homan, Attridge & Wardle 2001; Homan & Lister 2006; Vitrishchak et al. 2008; Papers IV, V).

The beaming phenomenon gives life to another model that resolves one more

inconsistency in the AGN behaviour. Some blazars emit high energy radiation up to TeV. The nature of the high-energy emission in blazars will be touched later in this introduction (see section 4.4.2). The Doppler-factors required for the production of the high-energy emission are high ($\delta \geq 50$), which is in disagreement with the values of Doppler factors observed by VLBI ($\delta \sim 15$) in the TeV blazars (Georganopoulos & Kazanas, 2003). This disagreement was resolved by Ghisellini, Tavecchio & Chiaberge (2005) who suggested that AGN jet must be stratified, with the fast moving inner part ('spine') and a decelerating outer layer ('sheath'). The slower moving sheath sees the Doppler-boosted radiation from the spine, which enhanses the production of the high-energy emission. The *spine-sheath model* is used in the magnetohydrodynamical simulations of jets (e.g., Keppens et al., 2008).

4.3.1 Linear polarization

Detection of LP in AGN jets suggests that the mechanism of radiation is synchrotron (discussed in more detail in the section 4.4.1). Generation of synchrotron emission requires the presence of a magnetic field and relativistic charged particles in the jet. EVPA, the electric vector position angle also known as the linear polarization position angle, χ, is defined as the angle between the projected direction of the electric field vector on the sky plane and direction to the north.The direction of an electric vector is perpendicular to the magnetic vector direction in the regions where the emission is optically thin. In the regions where the synchrotron self-absorption plays a significant role, the electric vector is parallel to the direction of the magnetic field. In Paper I we utilized this property of the synchrotron radio emission and figured out that among blazars there are sources having both optically thick and optically thin VLBI cores. We also found that synchrotron emission in the optical and radio domains comes from the same spatial region in the inner jet, or from two neighboring regions with similar configuration of the magnetic field. If radiation on its way to the observer passes through a region with thermal plasma entangled with a magnetic field (so called *Faraday screen*), the EVPA changes. Electric vector rotates by an amount (in radians):

$$\Delta\chi = 7.27 \times 10^4 [\nu(1+z)]^{-2} \int n_{\rm e} B_{\parallel} ds \, , \tag{4.7}$$

where ν is the frequency of radiation in GHz, z is the redshift of the AGN, $n_{\rm e}$ is the electron density in the Faraday screen, $B_{\parallel}$ is the component of the screen magnetic field that is parallel to the line of sight, and ds is the length of the light

path through the screen in parsecs. Multi-frequency observations are needed to detect Faraday rotation. Faraday rotation that is found in single-dish observations has Galactic origin for the majority of blazars. In Paper I, we present maps of Faraday rotation that were obtained with VLBI for six sources in our sample. The Faraday rotation distribution across the source is a result of the relative differences in the path of the polarized light through the plasma of the source itself. Radiation from the base of the jet passes through the plasma of the jet on its way to the observer, and experiences Faraday rotation. It is possible to recover the properties of the jet's magnetic field from the Faraday rotation gradient (e.g., Reichstein & Gabuzda, 2011; Mahmud, Gabuzda & Bezrukovs, 2009). However, the effect of Faraday rotation is decreased by the reciprocal of the Lorentz factors of the jet γ_j. In addition to that, there are two complications: 1) polarized radiation comes from different parts of the jet, thus its path in the screen differs for different regions of the source, and 2) magnetic field component along the line of sight is different in different regions. The net effect of these two factors is that different polarization vectors cancel each other, causing so called *Faraday depolarization*. The theoretical limit for LP of incoherent Synchrotron radiation in the uniform magnetic field depends on the energy distribution of emitting particles, and for the conditions exist in AGN jets a degree of the LP can reach ~ 70 % (Rybicki & Lightman, 2004). This value could be reached only in a fully ordered magnetic field, as amount of disorder leads to depolarization. In the majority of AGN, the degree of LP is on the order of several percent, which is an evidence for a highly disordered magnetic field. However, in some cases the local LP degree in the individual jet components may be very high, up to 50 % (Lister, 2001; Lister & Homan, 2005), and in rare cases can reach values very close to the theoretical limit (Cawthorne et al., 1993). That suggests, that in certain regions of the jet an ordered magnetic field dominates. The fractional polarization of jet components increases with their projected distance from the VLBI core along the jet (Lister, 2001).

4.3.2 Circular polarization

The synchrotron mechanism can also generate small quantity of CP. The gain transfer method of D. Homan and J. Wardle, described in section 2.3.6 of this thesis, was inspired by the pioneering theoretical work by Jones & O'dell (1977), who discussed this aspect of Synchrotron radiation, and also by the simulations of the linear and circular polarization in relativistic jets by Jones (1988).

Wardle & Homan (2003) considered possible theoretical mechanisms of CP generation in AGN jets. The most plausible candidates are the *direct Synchrotron generation* and *Faraday conversion* from LP. Intrinsic synchrotron CP depends on the component of the magnetic field which is perpendicular to the line of sight, and it decreases with the increase of disorder in the magnetic field. If a jet contains pair plasma, its electrons and positrons produce CP of the opposite sign that cancel each other, thus, in the electrically neutral pair plasma (where the number of electrons is equal to the number of positrons) intrinsic CP is equal to zero. The direct synchrotron mechanism of CP production would work only in electron-proton plasma. However, taking into account the amount of disorder inferred from LP observations, the amount of depolarization in the directly produced CP should be very high. The spectrum of directly generated CP (m_c denotes the degree of CP) is $m_c \sim \nu^{-1/2}$, for a homogeneous source (Wardle & Homan, 2003; Vitrishak, 2008) and is flat for a model of narrow conical relativistic Blandford - Königl jet. A more likely mechanism of CP generation in AGN jets is the Faraday conversion of LP into CP (see Wardle & Homan, 2003, for details). It is a birefringence effect in a magnetic field, when the two components of linearly polarized radiation, transverse and parallel to the magnetic field, have different speed. On their way through magnetized plasma, they gain a phase difference that corresponds to the circular polarization. However, synchrotron radiation in a uniform magnetic field produces only stokes Q or $-Q$, so additional Faraday rotation is needed in order to create both components of the LP vector. There are two modes of LP-CP conversion: one is due to internal Faraday rotation in the source, and another is due to spatial variations of the magnetic field direction. The first mode requires the presence of either electrons or positrons but not both, and it is, thus, operating only in the electron-proton plasma, as does the direct synchrotron mechanism of CP production. The second mode depends neither on the sign of electric charges of the emitting particles, nor on the direction of the magnetic field, so it may equally occur in electron-proton plasma or pair plasma. The spectrum of conversion CP is also flat in the Blandford-Königl model (see section 4.5.3). In a non-isothermal, case the spectra of both internal and converted CP are inverted, $m_c \sim \nu$. It is reported that CP is naturally produced via conversion in the helical magnetic field (Gabuzda et al., 2008).

4.4 Spectrum

Compact jets radiate in a broad range of photon energies, from radio to γ-rays. The spectral energy distribution (SED) curve of AGN has a characteristic 'two-humped' shape (see Fig. 4.1). Radio emission at low frequencies is dominated by synchrotron radiation from an extended jet, while synchrotron radiation from a compact jet produce most of the GHz to optical flux. The accretion disk is emitting thermal radiation in the ultraviolet, and inverse Compton scattering of radio photons by relativistic electrons in the compact jet produce most of the X- and γ-rays. Detailed considerations of radiative processes in AGN jets is beyond the scope of this thesis. A comprehensive discussion of the physical principles behind these phenomena and derivation of formulas can be found in a book 'Radiative processes in astrophysics' (Rybicki & Lightman, 2004), chapters 6 and 7.

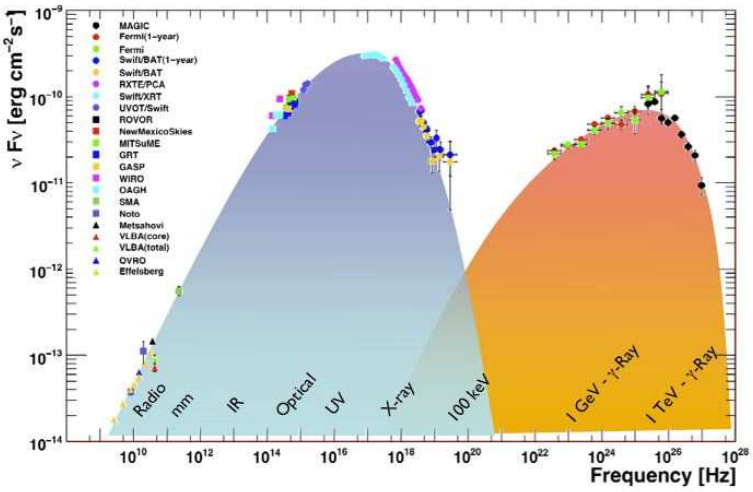

Figure 4.1: The SED of the blazar Markarian 421. Colors illustrate the synchrotron (blue) and inverse-Compton (orange) peaks. The data are taken with a number of different instruments during the observational campaign in 2009. Credit: Dr. Antonio Stamerra, http://www.pi.infn.it/ stamerra/.

4.4.1 Synchrotron component

Synchrotron radiation is emitted by charged particles accelerated in a magnetic field. The particle, initially moving angularly to the magnetic field, changes its motion due to the magnetic force and starts to circle around a field line. The component of velocity that is parallel to the field direction is retained, so that the trajectory of the particle becomes helical. As any accelerated charge, a particle in a magnetic field emits radiation. If the emitting particle is non-relativistic, the radiation is called *cyclotron*. In the case of a relativistic emitting particle, radiation is *beamed* in the direction of motion, i.e. concentrated in a narrow cone directed along the vector of its instant velocity. Less massive particles are more efficient in producing synchrotron radiation, so it is generally assumed that synchrotron radiation from AGN jets is generated by electrons. An observer sees a net emission of an ensemble of particles, which is described in terms of their energy distribution. Electrons are assumed to have a power-law energy spectrum, $N(E) = N_0 E^{-s}$. In the optically thin region, the net spectrum of a set of particles has the shape

$$S_\nu \propto \nu^{-(s-1)/2} \, . \tag{4.8}$$

At low frequencies, synchrotron emission is affected by synchrotron *self-absorption*. Below the *turnover* frequency ν_m the spectrum has the shape

$$S_\nu \propto \nu^{5/2} \, . \tag{4.9}$$

Due to radiative losses at higher frequencies, the energy distribution of electrons steepens. The steady-state distribution becomes $N(E) = N_0 E^{-s+1}$, which leads to the steepening of radiation spectrum:

$$S_\nu \propto \nu^{-s/2} \, . \tag{4.10}$$

Synchrotron emission is highly polarized, and the degree of polarization depends on the properties of magnetic field and energy distribution of electrons. In a uniform magnetic field, the degree of polarization of optically thin synchrotron radiation is

$$m_L = \frac{s+1}{s+7/3} \, . \tag{4.11}$$

In AGN jets the value of s typically is $> 70\%$.

4.4.2 Inverse Compton component

There are two models which explain the source of high energy emission in AGN. The *leptonic* model assumes that the second peak in the AGN SED (see Fig. 4.1) is formed by *inverse Compton scattering*. In this process, photons collide with relativistic electrons and gain energy from these collisions, thereby radiation is transferred to higher frequencies. If the seed photons are the same that were emitted by the synchrotron process in the jet, the mechanism of the high energy emission generation is called *synchrotron self Compton* (SSC) (Marscher & Gear, 1985; Boettcher, Mause & Schlickeiser, 1997). However, the seed photons may have originated from other sources, e.g. they could be thermal photons from the accretion disc, obscuring dust, or emission line photons from BLR clouds (Dermer, Schlickeiser & Mastichiadis, 1992; Sikora, Begelman & Rees, 1994). In this case, this mechanism is called *external inverse Compton* (EIC).

The alternative mechanism for the generation of high energy emission is called *hadronic*. It suggests that the second peak of the SED arises from synchrotron radiation of *protons* and *muons*. However, this model requires magnetic fields on the order of tens of gauss, and an acceleration of protons to the energies at which pions could be produced. Details of existing models of high energy emission production can be found in Mücke et al. (2003) and in the references therein. The leptonic model is in a better agreement with observed data, hence the inverse Compton nature of the second peak in AGN SED is now commonly accepted.

4.5 Physical processes in jet plasma

Observations and computer simulations suggest that the processes, determining the behavior of AGN jets, are magnetohydrodynamics (MHD), gas dynamics, plasma physics and, probably, electrodynamics. In this section, I give a short outline of the physical processes behind the observed phenomena in jets.

4.5.1 Jet launching and magnetic field

Observations of highly collimated (jet opening angle is $< 1^{\circ}$), fast ($\gamma > 10$) (e.g., Jorstad et al., 2005) jets and evidence for the presence of a *helical magnetic field* in blazar jets (Asada et al., 2002; O'Sullivan & Gabuzda, 2009; Gabuzda et al., 2008; Lyutikov, Pariev & Gabuzda, 2005, and references therein) lead to a conclusion that jets are launched by a magnetic mechanism. Differential rotation of the accretion disc or/and the black hole winds up the polar magnetic field

lines forming a helical magnetic field structure. The toroidal component of this field creates a hoop stress, which squeezes plasma towards the axis of the helix, thereby collimating the jet. The magnetic field strength decreases with the distance from the black hole creating a pressure gradient, which supports the flow (Vlahakis & Königl, 2004). The inner jet is Poynting-flux dominated, at some distance from the core it becomes matter-dominated (see Sikora et al., 2005, and references therein for details). Magnetic flux in the jet is conserved with increasing distance from the central engine. Under this condition the component of the field parallel to the jet axis is inversely proportional to the square of distance from the SMBH: $B_{\parallel} \sim 1/R^2$, and the transverse component decreases with distance as $B_{\perp} \sim 1/R$. Beyond the acceleration and collimation zone, current-driven instabilities break the order in the field and tangle it. The velocity shear stretches the helical field and aligns it with the jet axis, or creates turbulence which disorders the field.

4.5.2 Shocks and instabilities in the jet

If the energy density of the magnetic field in the jet is lower than that of the particles, the magnetic field 'freezes in' and follows plasma in its motion. In this case, the jet behaves like a gas flow, thus a gasodynamical approach could be used. Interaction of the jet with ambient interstellar medium causes the generation of sound shock waves and changes the jet cross-section due to the boundary pressure difference (Bogovalov & Tsinganos, 2005; Daly & Marscher, 1988). In a circularly symmetrical jet, shock waves have conical shapes. If the pressure difference is $\geq 50\%$, oblique shocks are formed and re-collimate the jet. Shocks could also emerge due to internal causes: if the flow speed is changing abruptly or mass/energy injection from the central engine takes place. The relative velocity of this perturbation with respect to the flow must be supersonic in order to create a shock wave. If the flow speed is relativistic, the Lorentz factor of the initial perturbation must be at least two times higher than the speed of the underlying flow. Near the base, however, the energy of the magnetic field overrides the energy of the particles, and on the parsec scale it is likely that the two energies are in equipartition. In this case, the jet should be considered as a magnetohydrodynamical system. If the toroidal component of the magnetic field dominates, kink instabilities develop in the jet leading to the formation of strangulation-like perturbations (e.g., Begelman, 1998). Due to their high *Mach numbers* (a Mach number is a dimensionless dynamical parameter that characterises the flow, it is equal to the ratio of the jet speed to the sound speed in the ambient medium, $M = v_{\rm flow}/c_{\rm s}$),

Lorentz factors and strong magnetic field jets of powerful sources, for example, FRII quasars and radio galaxies, can propagate undisturbed up to distances of $\sim 10^5$ pc. However, if a jet propagates in a relatively dense environment, it is subjected to instabilities such as Kelvin-Helmholtz, that occur in the presence of velocity shear or velocity difference on the boundary between two moving fluids (Hardee, 2006). These instabilities manifest as oscillations of the transverse radius of the jet and departure from the axial symmetry. Instabilities may lead to the development of turbulence in the jet or the formation of a shock. They are most likely responsible for features that could be observed on the parsec and kiloparsec scales, and probably also for the flaring activity of blazars (Sikora et al., 2005).

4.5.3 Jet components

As it was mentioned in sections 4.2 and 4.2.1, some AGN jets consist of bright components, which are moving down the stream with superluminal apparent velocities, or reside at the same place in the jet for a long time. These bright features must be the regions where the electron density and/or magnetic field strength are higher than that of the ambient jet. However, the nature of the jet components, i.e. the cause of these 'enhancements' of the electron density and the magnetic field, is not entirely clear. There are several models trying to reproduce VLBI jets appearance, evolution and spectra. According to the most popular hypothesis, they are shocks propagating in the jet plasma, which are caused by disturbances in the base of the jet. Electrons are accelerated to relativistic speeds via the first-order Fermi process (Marscher & Gear, 1985; Gomez, Alberdi & Marcaide, 1993, 1994; Gomez et al., 1994). According to another hypothesis, these brightness enhancements are clouds, or 'blobs', of dense turbulent plasma traveling along the jet. Electrons in these clouds are possibly accelerated via the second-order statistical Fermi process. There are several models, explaining the jet components in this way (see Despringre & Fraix-Burnet 1997 for the the *two-fluid model* and Celotti & Ghisellini 2008, Inoue & Takahara 1996 for the *one-zone synchrotron-inverse Compton model* of high energy emission). Progenitors of the moving 'blobs' are considered to be perturbations at the jet origin, as for the shock waves. The third main model attribute bright knots and filaments in jets to Kelvin-Helmholtz instabilities (Perucho et al., 2006; Perucho & Lobanov, 2007). Due to the sparsity of VLBI observations and insufficiency of their angular resolution, the unambiguous identification of nature of the jet components is not possible at this moment. Comparison of the observed behavior of components with the results of numerical magnetohydrodynamical simulations is the mail tool for disentangling

this puzzle. It may also happen that jet components of all three classes are present in AGN jets. The 'leading' hypothesis at this moment is the one of shocks propagating in the jet. This model allows quantitative consideration of the phenomena, observed in the jet due to the motion of the component, without delving deeply into the question of their origin. In other words, this model answers the question "How?" - without going deeply into "What?" and "Why?" A detailed discussion of this model is given in the following subsection.

Stationary components are discussed in detail in Jorstad et al. (2001). This paper offers three possible models for the stationary components: (1) standing recollimation shocks, (2) regions of the maximum Doppler beaming, i.e. when the bending jets point exactly towards the observer, (3) standing shocks due to the sharp bend of the jet, caused by interaction of the jet with the overdensity in the ambient medium.

Theoretical framework: a conical relativistic jet with propagating shocks

In the 1970s, the variable polarized emission from compact radio sources was interpreted as incoherent synchrotron radiation from a set of relativistic electrons with a nonthermal energy distribution. The first consistent model of emitting plasma behavior in theese sources was proposed by R. D. Blandford and A. Königl in 1979. They show that the observed variability and kinematics of the compact radio source can be explain by the model of a quasi-steady collimated conical supersonic relativistic jet (Blandford & Königl, 1979). This model gives a good approximation of the real shape of a relativistic AGN jet, and is referred to as the *Blandford - Königl model*. The observed brightness enhancements in this model are attributed to the strong shock waves propagating in the jet, or dense clouds accelerated by the flow. Unfortunately, Blandford-Königl model did not consider the physics of the shocks and/or in detail. In 1985, Marscher & Gear (1985) suggested a detailed semi-quantitative description of the radio emission from strong and moderate shocks propagating down the jet, and considered the conditions in jet plasma. The shocks are caused by the presence of pressure gradients in the jet. This so called *shocked jet model* was able to describe in general the time and spectrum evolution of the source during the flare, which is observed in wavebands from the radio to optical, and predicts the connection of AGN radio outbursts with high energy emission. This theoretical framework, known as the *shock-in-jet scenario*, is still valid and widely used to describe AGN behavior. Fig. 4.2 schematically demonstrates the plethora of events taking place in the central region of an AGN, explained within the framework of the Blandford - Königl model and shock-in-

jet scenario. All these events are connected to the generation and propagation of shocks in jet.

Evolution of the shock in the jet

The shocked jet model of Marscher and Gear, however, lacked details of the spectral evolution of an AGN source. The data from the multifrequency (submillimeter to centimeter) single-dish radio monitoring of AGN flux densities yields a bulk of new information every year. Radio light curves of AGN demonstrated relatively frequent flares, which were attributed to the generation and propagation of a shock wave in the jet. Comparison of AGN behavior at different frequencies revealed that flares appear differently for different sources, and even two flares of the same source may not be similar. In some cases, the flux density peaks at different frequencies are delayed with respect to each other, in others they appear simultaneously at all observed frequencies. Also, dependence of a peak flux density on frequency $S_{\rm peak}(\nu_{\rm obs})$ was ambiguous. It was argued, if different flares have different nature, or they are manifestations of the same intrinsic process in AGN.

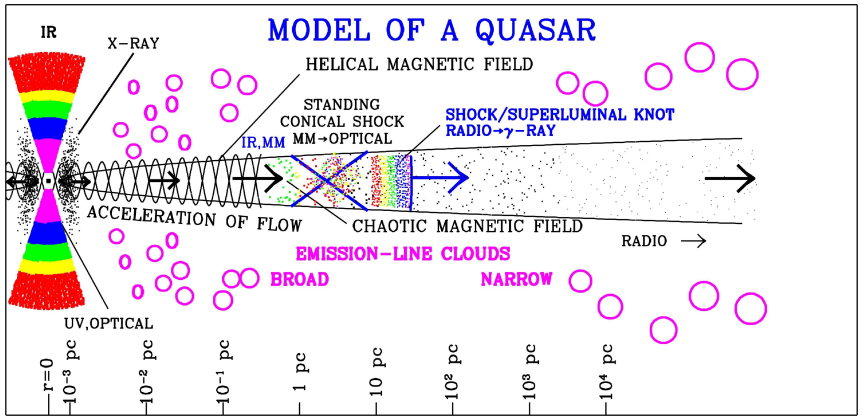

Figure 4.2: Sketch of AGN structure and the location of regions where emission is generated. This is the side view, the SMBH and accretion disk are located at the left side of a plot, a conical relativistic jet is propagating to the right. Colors represent different frequencies, the scale is logarithmic, in parsecs. Credit: Dr. Alan Marscher, http://www.bu.edu/blazars/research.html.

Valtaoja et al. (1992) proposed a *generalized shock model* that explained different flares within the same theoretical framework. According to them, each propagating shock has three stages: the growth, the plateau and the decay. The spectrum of the shock has the same synchrotron shape during all stages of evolution (see section 4.4.1 and Fig. 4.1), however, the turnover frequency ν_m and turnover flux S_{ν_m} change with time. The turnover frequency decreases during the whole period of the shock evolution. The flux increases during the growth stage, stays the same during the plateau phase and decreases at the decay stage. All shocks evolve in the same way, and the appearance of the accompanying flare and its visibility on the VLBI map depend on the fact whether the observing frequency $\nu_{\rm obs}$ is lower or higher than ν_r, the turnover frequency at the moment when the maximum flux density is reached (in other words, at the end of the growth stage).

4.5.4 Mass content

The term 'plasma' as jet constituent was used, in this, text in the majority of cases, without mentioning the actual particle content. The reason is that in spite of many years of theoretical and observational studies, the actual particle composition of the AGN jet plasma is not known. It it clear that synchrotron emission must be caused by light charged particles, presumably *electrons*. The second component that makes the plasma electrically neutral is arguable: it must consist of either protons or positrons. However, by now, there is no any reliable observational test of the AGN jet plasma content. All existing methods give ambiguous results because of the lack of either sensitivity or statistics. Spectral and multi-frequency observations, high-energy emission and circular plus linear polarization are the observables which can shed light on this question together with SED modeling. Theoretically, an AGN jet is composed of the matter that was blown off the surface of an accretion disc, so it must contain a fair amount of normal matter, namely electron-proton plasma. However, in the Poynting-flux dominated jets electron-positron pairs can be generated as a product of interaction of high-energy photons with the electromagnetic field. In reality, it is likely that AGN jets contain a mixture of both types of plasma (Wardle et al., 1998; Celotti & Ghisellini, 2003, 2008).

Chapter 5

Conclusions and summary of publications

The introduction to this thesis represents an overview of several relatively broad topics, which are closely related to the research I carried out during my postgraduate studies. These basics are crucial for the understanding of the results that are published in the attached papers.

Chapter 2 contains the basic theoretical description and technical details of VLBI, the observational technique which was used to obtain the scientific data. In Chapter 3, I present a short overview of AGN, the class of astrophysical objects which were studied and in Chapter 4, one can find a more detailed description of the physical processes that take place in the relativistic jets, the part of AGN which is visible in the radio domain. In this Chapter I justify the choice of methods for AGN research, familiarize the reader with some useful multifrequency VLBI practicalities and give a short overview of the original publications.

5.1 Multifrequency VLBI observations' 'whys' and 'hows'

AGN are compact radio sources, as it is suggested by their rapid variability. Let us estimate the angular size of a typical blazar, from radio variability monitoring with a single dish. The variability parameters which are used in this estimation can be obtained from the analysis of the source light curve. The luminosity of AGN changes drastically on the time scale of t_v, which is on the order of several months, for an average blazar. The source size can not exceed the distance that light travels during this time interval, $R \leq ct_v$, where c is the speed of light. If one takes into account the relativistic beaming of the plasma in the jet, which is moving towards the observer, and accounts for the contraction of length in the direction

of motion, the intrinsic size of the emitting region becomes $R_{\rm in} \leq \delta c t_{\rm v}$, where δ is the Doppler-factor of the plasma (Lang, 2006). Let us consider, for simplicity, a spherical emitting region, which implies that the transverse size of this region, which is the apparent size of the source, is also equal to $R_{\rm in}$. For a relatively close extragalactic object with known redshift, z, we can estimate the distance D to the object using the Hubble law: $D = zc/H_0$, where $H_0 = 71\ \frac{\rm km}{\rm s}/Mpc$ is the Hubble constant. The apparent angular size of this emitting region, in this case, is:

$$\phi \simeq \frac{R_{\rm in}}{D} = 8.3 \cdot 10^{-14} \frac{H_0 t_{\rm v}}{z}\ \ rad = 1.7 \cdot 10^{-5} \frac{H_0 t_{\rm v}}{z}\ \ mas\ , \qquad (5.1)$$

if the variability time scale $t_{\rm v}$ is measured in months.

For example, for the blazar S5 0716+714, which is discussed in Papers II, III and V, $z = 0.31$ (Nilsson et al., 2008), and the Doppler factor derived from the monitoring of variability at 22 and 43 GHz is $\sim$11 (Hovatta et al., 2009). Strong flares occur on the time-scales of years. The median duration of a flare at 37 GHz for this source from Hovatta et al. (2008) is $\sim$3.1 years. Taking into account these parameters, we obtain a typical value for the angular size of the emitting region in this source to be $\phi \simeq 1.6$ mas. This is the value which is accessible only with interferometry. Most blazars are rather faint objects at all observed wavebands, therefore, speckle imaging, for example, can not be used. Thus, VLBI is the only technique which can resolve these objects. It is also worth mentioning that many blazars, including 0716+714, demonstrate fast variability on timescales of days and even shorter (e.g., Wagner & Witzel, 1995; Gorshkov et al., 2011). However, relative flux changes in such fast events are not high. For example, the rate of changes reported by Wagner & Witzel (1995) for 0716+714 were about 5 % per day in the course of several days.

The advantages of multifrequency VLBI observations are the broad range of observing frequencies, and possibility to access different parts of the AGN jet at different wavebands. However, each frequency band has its own angular resolution. As it was mentioned in section 2.1, the resolution of an interferometer is $\propto \lambda/B_{\rm max}$, where λ is the observing wavelength, and $B_{\rm max}$ is the maximum baseline of the interferometer. More precisely, resolutionin milliarcseconds is $\simeq 2063 \cdot \frac{\lambda[\rm cm]}{B_{\rm max}[\rm km]}$ (NRAO, 2011). In my studies, I used the data observed with the Very Large Baseline Array[1]. The VLBA has ten 25-meter parabolic antennas, and it covers the territory of the United States with a maximum baseline of $\sim$8000 km. The observing bands of the VLBA lie in the centimeter range. The

[1]VLBA, homepage can be found at `http://www.vlba.nrao.edu/`

Table 5.1: VLBA bands used for observations analyzed in this thesis: identifier, frequency, wavelength, angular resolution.

ID	ν, [GHz]	λ [cm]	Θ [mas]
W	86	0.3	0.12
Q	43	0.7	0.17
K	22	1	0.32
U	15	2	0.47
C	5	6	1.4
L	1.6	18	4.3

information about the observing bands that were used to acquire data which were then published in Papers I-V is summarized in Table 5.1. The shape and size of the synthesized clean beam, which is the PSF of the interferometer, are slightly different at different epochs due to the difference in the uv-coverage, however, its size is always very close to the nominal resolution. For example, in Paper III, we carried out the kinematic study of the blazar 0716+714, for which we had to compare VLBA images of this source taken at different epochs. In order to unify these images, we convolved the final model of the source at each epoch with the same clean beam with a size of 1.5×2.5.

Blazar jets emit optically thin synchrotron emission. The spectrum of such emission is inverted with frequency, i.e. at lower frequencies the jet looks brighter than at higher frequencies. Also, the further is the plasma from the core, the lower is the turnover frequency, which leads to the situation that the large-scale jet 'fades away' at higher frequencies, and the observer sees only the inner jet and the VLBI core. In this way, on the VLBI maps at lower frequencies (1.6-5 GHz), one can see a part of extended emission from the blazar. For the blazar 0716+714, the large-scale jet has an apparent size of 12 mas. At higher frequencies (15-43 GHz), inner jet ($\sim$1-6 mas), situated deeper, opens up. Large-scale jet at high frequencies, in most cases, fades away, however, certain jet components may have a higher turnover frequency than the ambient plasma does, so on the high-frequency VLBI image such source appears to have a 'double-' or 'multiple-

source' structure, where the VLBI core is the brightest spot and jet components appear much fainter. See Fig. 2 in Paper I for several examples of VLBA maps of blazars at 43 GHz. At the highest frequency, for example, on 86 GHz (3 mm) VLBI images, one can see very deep into the inner jet, and many blazars become rather compact. One can compare Fig. 1 from Paper II and Fig. 1 from Paper III to see the difference in appearance of the blazar 0716+714 at 43 and 5 GHz, or Figs. 1 and 2 in Paper V for comparison of images at 5 and 22 GHz.

5.2 Summaries of papers

The papers presented in this thesis are not a part of one big consistent project, they are a collection of smaller projects, and could be compared to separate pieces of a large complicated puzzle: each paper contributes to one particular aspect of AGN studies. Since all the papers were written in collaboration with other researchers, I refer to the group of authors as 'we'.

5.2.1 Paper I

Paper I probes the question of the existence of cospatial optical and radio synchrotron emission in AGN jets. According to the standard model, optical emission comes from the jet part that is in a very close vicinity of the black hole. However, some models allow optical and radio emission to be generated in the same region for the narrow range of jet plasma parameters (e.g., inhomogenious SSC model of Ghisellini, Maraschi & Treves, 1985). Observational verification of this spatial coincidence of radio and optical emission is difficult due to a different resolution in these two wavebands. However, comparing the direction of polarization vectors in the optical and on the VLBI map, one can find the region on the VLBI map where they are aligned. That means, that optical emission comes from the same place as the aligned radio emission. They either both come from the same spatial region, of from the two separate regions with the same orientation of the magnetic field. The second is less likely, since the magnetic field in the inner jet is expected to be strongly tangled.

We investigate the connection between the optical and radio emission of 12 AGN. We analyzed simultaneous polarization VLBA observations of the sources at 15, 22 and 43 GHz and the quasi-simultaneous optical polarization observations. We compared EVPA of the radio polarization in the VLBI cores between frequencies. Some sources demonstrated Faraday rotation in the core, for them we calculated a 'zero-wavelength' EVPA χ_0, formally extrapolating the found

amount of Faraday rotation to $\lambda = 0$, and compare them to the optical ones. This allowed us to exclude influence of local cloud magnetized plasma, and to make sure that we compare the EVPA in the optically thin Synchrotron regime in both optical and radio. Also it yielded the core Faraday rotation measures for six objects as a side product of this project. If the radio EVPA were stable over all three radio frequencies, we compared them directly to the optical one. In some sources, there was a clear 90° rotation of the VLBI core EVPA at one or two lowest radio frequencies (15 or/and 22 GHz), with respect to one at 43 GHz. This is an indication that the emission regime changes from the optically thin to the optically thick between two observing bands, since the turnover frequency ν_m lies between them. For such sources, we used the radio EVPA obtained at 43 GHz without any changes, and those at lower radio frequencies were rotated by 90° for the analysis.

We found that the optical EVPA coincides with the EVPA of the optically thin radio emission from the VLBI core, for all but 2 sources, within the uncertainty of 30°. This is an indication that in the majority of AGN optical and radio emission is cospatial, and comes from the inner part of the relativistic jet (VLBI-core).

5.2.2 Papers II and III

Papers II and III present the kinematic analysis of the blazar 0716+714 during an active state. This bright, violently variable blazar had an optical outburst in the end of 2003, and a radio one in March 2004. A multifrequency campaign was triggered by the first outburst. We used VLBI observations at 1.6, 5, 22, 43 and 86 GHz at five epochs before and after the major radio outburst in March 2004. For the inner jet (0-1 mas), kinematic studies using the frequency bands W, Q and K, were used.

For the four last epochs, the source was observed as frequent as once a month. We made detailed VLBA images of the source and modeled the jet with Gaussian components. Images at different frequencies were analyzed separately and independently. However, the position of components found at those three frequencies agreed within two sigma. In the jet of 0716+714, we identified three moving and one stationary component. Estimated ejection times (more precisely, the moments of crossing the VLBI core) coincided within one sigma with the moments of the beginning of the 37 GHz peaks on the total flux density curve. It is worth mentioning, that during this period there was one more 37 GHz peak, however, it did not lead to the formation of a VLBI component. It is in line with the generalized model of shock evolution by Valtaoja et al. (1992). This flare is likely to be the so called *high-peaking flare*, when the shock reaches its maximum development well

above 37 GHz, so it is observed at the last decaying stage and is already too faint to be seen with VLBI.

The inner jet of 0716+714 demonstrated fast superluminal motion with apparent speeds of 8-19*c*. The jet was resolved in the transverse direction, and the jet components were moving along the wiggling trajectories, which can be a manifestation of helical motion.

The large-scale (1-12 mas) jet kinematics of 0716+714 is a topic of Paper III. We imaged 0716+714 at six epochs at 5 GHz using two different methods: a conventional method and a MEM-based algorithm, GMEM, developed and realized by A. Baikova in the package VLBImager. The large-scale jet of 0716+714 appears as a continuous flow of plasma with a very bright point-like core and a featureless jet. This type of structure is difficult to reproduce with a conventional CLEAN. However, GMEM has proven to reconstruct simulated sources of this type successfully. The theoretical foundations of GMEM are also presented in the paper.

Both the conventional method and GMEM yielded similar kinematic results: the large-scale jet of 0716+714 is mostly stationary, unlike the inner jet, and much fainter. We try to explain this discrepancy of in the apparent velocity by the hypothesis that the jet of 0716+714 has turned away from the observer at the projected distance of 1 mas from the VLBI core, changing the angle to the line of sight from $\sim 5^\circ$ in the inner region to $\sim 11^\circ$. The difference in the amount of beaming caused both apparent deceleration and dimming of the components.

5.2.3 Papers IV and V

These papers address the parsec-scale circular polarization of AGN. Paper IV presents results of the analysis of the 15, 22 and 43 GHz polarization VLBA observations of 41 AGN. Polarization data were calibrated using the gain transfer method in order to obtain CP images. The details of data reduction and results verification are also presented in the paper.

The parsec-scale CP was detected in 17 sources, including eight first time detections. In the sources where CP was detected not for the first time, the results were consistent with previous observations. In ten sources, the CP was detected at more than one frequency. However, no clear picture of the frequency dependence of the CP is seen, so based on this data only, there is no chance to argue about the possible mechanisms of CP generation, and, therefore, plasma mass content. Nevertheless, the possibility of the Faraday conversion is discussed in context of observed transverse structure of the parsec-scale CP.

Paper V is a continuation of the CP topic. In this paper we attempt to apply the gain transfer method (GT) to the single-source VLBA experiment. Our observations of 0716+714 were optimized for studying one object, with a short observing time and a low number of observed calibrators. For this reason, we could not use a combined gain curve. Instead, we transferred gains from the possibly circularly unpolarized calibrator 0420-014, using only two scans of this source. We discussed possible sources of errors of the resulting CP value and contribution of each of them, and found them within the limits needed for the CP imaging. Measurements of the circular polarization were made at three epochs, separated by approximately two months, at frequencies of 5 and 22 GHz. The the first epoch coincided with an ejection of a new superluminal jet component.

We detected moderate positive circular polarization at the VLBI core at two last epochs at 5 GHz with significance level of 5 and 3 sigmas. At 22 GHz, the CP had been mapped, but did not satisfy the 3 sigma detection condition. At 5 GHz, we found CP values of $+0.32\pm0.06$ and $+0.20\pm0.06$. These values are consistent with the previous measurements for this source (Homan & Lister, 2006).

In addition to the CP, we considered the LP of 0716+714 at these three epochs. We found that at 5 GHz the minimum of LP in the VLBI core and EVPA rotation at $\sim 50^{\circ}$ coincided with the minimum/non-detection of the CP, and with the ejection of the new jet component. LP EVPA rotation at 22 GHz was also detected, but was not connected to any other events.

It has to be underlined that Paper V is submitted for publication in *Astronomy & Astrophysics*, however, the final accepted text and conclusions may differ from the submitted version due to the suggestions of the referees.

Bibliography

Ables J. G., 1974, A&AS, 15, 383

Agudo I., Thum C., Wiesemeyer H., Krichbaum T. P., 2010, ApJS, 189, 1

Ambartsumian V. A., 1958, in La Structure et L'Evolution de L'Univers, Proc. XI Solvay Conference

Antonucci R., 1993, ARA&A, 31, 473

Asada K., Inoue M., Uchida Y., Kameno S., Fujisawa K., Iguchi S., Mutoh M., 2002, PASJ, 54, L39

Baikova A. T., 2007, Astronomy Reports, 51, 891

Beckwith S. V. W. et al., 2006, AJ, 132, 1729

Begelman M. C., 1998, ApJ, 493, 291

Begelman M. C., Blandford R. D., Rees M. J., 1984, Reviews of Modern Physics, 56, 255

Bennett A. S., 1962, MmRAS, 68, 163

Blandford R. D., Königl A., 1979, ApJ, 232, 34

Boettcher M., Mause H., Schlickeiser R., 1997, A&A, 324, 395

Bogovalov S., Tsinganos K., 2005, MNRAS, 357, 918

Bridle A. H., Greisen E. W., 1994, The NRAO AIPS Project – A Summary. AIPS Memo 87, NRAO

Burke B. F., Graham-Smith F., 2010, Tools of Radio Astronomy, 3rd edn. Cambridge University Press

Cawthorne T. V., Wardle J. F. C., Roberts D. H., Gabuzda D. C., Brown L. F., 1993, ApJ, 416, 496

Celotti A., Ghisellini G., 2003, in Astronomical Society of the Pacific Conference Series, Vol. 290, Active Galactic Nuclei: From Central Engine to Host Galaxy, S. Collin, F. Combes, & I. Shlosman, ed., p. 327

Celotti A., Ghisellini G., 2008, MNRAS, 385, 283

Cenacchi E., Kraus A., Beckert T., Mack K., 2009, ArXiv e-prints

Clark B. G., 1980, A&A, 89, 377

Cohen M. H., Cannon W., Purcell G. H., Shaffer D. B., Broderick J. J., Kellermann K. I., Jauncey D. L., 1971, ApJ, 170, 207

Cohen M. H., Lister M. L., Homan D. C., Kadler M., Kellermann K. I., Kovalev Y. Y., Vermeulen R. C., 2007, ApJ, 658, 232

Conway R. G., Kronberg P. P., 1969, MNRAS, 142, 11

Cornwell T. J., Evans K. F., 1985, A&A, 143, 77

Cotton W. D., 1993, AJ, 106, 1241

Cotton W. D., 1995, in Astronomical Society of the Pacific Conference Series, Vol. 82, Very Long Baseline Interferometry and the VLBA, J. A. Zensus, P. J. Diamond, & P. J. Napier, ed., p. 189

Cotton W. D., Geldzahler B. J., Marcaide J. M., Shapiro I. I., Sanroma M., Rius A., 1984, ApJ, 286, 503

Daly R. A., Marscher A. P., 1988, ApJ, 334, 539

Dent W. A., 1965, Science, 148, 1458

Dermer C. D., Schlickeiser R., Mastichiadis A., 1992, A&A, 256, L27

Despringre V., Fraix-Burnet D., 1997, A&A, 320, 26

Edge D. O., Shakeshaft J. R., McAdam W. B., Baldwin J. E., Archer S., 1959, MmRAS, 68, 37

Fan J. H., Xie G. Z., Pecontal E., Pecontal A., Copin Y., 1998, ApJ, 507, 173

Fanaroff B. L., Riley J. M., 1974, MNRAS, 167, 31

Ferrarese L., Ford H., 2005, Space Sci. Rev., 116, 523

Frieden B. R., 1972, Journal of the Optical Society of America (1917-1983), 62, 511

Gabuzda D. C., Vitrishchak V. M., Mahmud M., O'Sullivan S., 2008, in Astronomical Society of the Pacific Conference Series, Vol. 386, Extragalactic Jets: Theory and Observation from Radio to Gamma Ray, T. A. Rector & D. S. De Young, ed., p. 444

Georganopoulos M., Kazanas D., 2003, ApJ, 594, L27

Ghez A. M., Klein B. L., Morris M., Becklin E. E., 1998, ApJ, 509, 678

Ghez A. M., Morris M., Becklin E. E., Tanner A., Kremenek T., 2000, Nature, 407, 349

Ghisellini G., 1999, in XIII National Meeting on General Relativity (SIGRAV)

Ghisellini G., Maraschi L., Treves A., 1985, A&A, 146, 204

Ghisellini G., Tavecchio F., Chiaberge M., 2005, A&A, 432, 401

Gomez J. L., Alberdi A., Marcaide J. M., 1993, A&A, 274, 55

Gomez J. L., Alberdi A., Marcaide J. M., 1994, A&A, 284, 51

Gomez J. L., Alberdi A., Marcaide J. M., Marscher A. P., Travis J. P., 1994, A&A, 292, 33

Gopal-Krishna, Dhurde S., Sircar P., Wiita P. J., 2007, MNRAS, 377, 446

Gopal-Krishna, Sircar P., Dhurde S., 2007, Journal of Astrophysics and Astronomy, 28, 29

Gorshkov A. G., Ipatov A. V., Konnikova V. K., Mardyshkin V. V., Mingaliev M. G., Finkel'Shtein A. M., Kharinov M. A., 2011, Astronomy Reports, 55, 97

Haggard D., Green P. J., Anderson S. F., Constantin A., Aldcroft T. L., Kim D.-W., Barkhouse W. A., 2010, ApJ, 723, 1447

Hardee P. E., 2006, in Astronomical Society of the Pacific Conference Series, Vol. 350, Blazar Variability Workshop II: Entering the GLAST Era, H. R. Miller, K. Marshall, J. R. Webb, & M. F. Aller, ed., p. 205

Hazard C., Mackey M. B., Shimmins A. J., 1963, Nature, 197, 1037

Heinz S., Sunyaev R. A., 2003, MNRAS, 343, L59

Högbom J. A., 1974, A&AS, 15, 417

Homan D. C., Attridge J. M., Wardle J. F. C., 2001, ApJ, 556, 113

Homan D. C., Lister M. L., 2006, AJ, 131, 1262

Homan D. C., Wardle J. F. C., 1999, AJ, 118, 1942

Hovatta T., Nieppola E., Tornikoski M., Valtaoja E., Aller M. F., Aller H. D., 2008, A&A, 485, 51

Hovatta T., Valtaoja E., Tornikoski M., Lähteenmäki A., 2009, A&A, 494, 527

Inoue S., Takahara F., 1996, ApJ, 463, 555

Jones T. W., 1988, ApJ, 332, 678

Jones T. W., O'dell S. L., 1977, ApJ, 214, 522

Jorstad S. G. et al., 2005, AJ, 130, 1418

Jorstad S. G., Marscher A. P., Mattox J. R., Wehrle A. E., Bloom S. D., Yurchenko A. V., 2001, ApJS, 134, 181

Kellermann K. I., Pauliny-Toth I. I. K., 1968, ARA&A, 6, 417

Keppens R., Meliani Z., van der Holst B., Casse F., 2008, A&A, 486, 663

Labeyrie A., 1970, A&A, 6, 85

Lacy M., 2003, in Astronomical Society of the Pacific Conference Series, Vol. 290, Active Galactic Nuclei: From Central Engine to Host Galaxy, S. Collin, F. Combes, & I. Shlosman, ed., p. 343

Lang K. R., 2006, Astrophysical Formulae: Space, Time, Matter and Cosmology, Vol. 2. Springer

Levanda R., Leshem A., 2010, IEEE Signal Processing Magazine, 27, 14

Lister M. L., 2001, ApJ, 562, 208

Lister M. L. et al., 2009, AJ, 138, 1874

Lister M. L., Homan D. C., 2005, AJ, 130, 1389

Lyutikov M., Pariev V. I., Gabuzda D. C., 2005, MNRAS, 360, 869

Mahmud M., Gabuzda D. C., Bezrukovs V., 2009, MNRAS, 400, 2

Marscher A. P., Gear W. K., 1985, ApJ, 298, 114

Meier D. L., 2002, NewAR, 46, 247

Merloni A., Heinz S., Di Matteo T., 2005, Ap&SS, 300, 45

Moran J. M., Dhawan V., 1995, in ASP Conference Series, Vol. 82, Very Long Baseline Interferometry and the VLBA, Zensus J. A., Diamond P. J., Napier P. J., eds., pp. 161–188

Mortlock D. J. et al., 2011, Nature, 474, 616

Mücke A., Protheroe R. J., Engel R., Rachen J. P., Stanev T., 2003, Astroparticle Physics, 18, 593

Nilsson K., Pursimo T., Sillanpää A., Takalo L. O., Lindfors E., 2008, A&A, 487, L29

NRAO, 2010, The AIPS Cookbook. NRAO

NRAO, 2011, Very Long Baseline Array observational status summary. http://www.vlba.nrao.edu/astro/obstatus/current

O'Sullivan S. P., Gabuzda D. C., 2009, MNRAS, 393, 429

Perucho M., Lobanov A. P., 2007, A&A, 469, L23

Perucho M., Lobanov A. P., Martí J., Hardee P. E., 2006, A&A, 456, 493

Peterson B. M., 2006, in Lecture Notes in Physics, Berlin Springer Verlag, Vol. 693, Physics of Active Galactic Nuclei at all Scales, D. Alloin, ed., p. 77

Peterson B. M., Wilkes B. J., 2000, Encyclopedia of Astronomy and Astrophysics, IOP

Piner B. G., Bhattarai D., Edwards P. G., Jones D. L., 2006, ApJ, 640, 196

Ponsonby J. E. B., 1973, MNRAS, 163, 369

Rayner D. P., Norris R. P., Sault R. J., 2000, MNRAS, 319, 484

Rees M. J., 1966, Nature, 211, 468

Reichstein A., Gabuzda D., 2011, arXiv:1102.0702

Roberts D. H., Gabuzda D. C., Wardle J. F. C., 1987, ApJ, 323, 536

Rybicki G. B., Lightman A. P., 2004, Radiative Processes in Astrophysics, 2nd edn. Wiley

Ryle M., Vonberg D., 1946, Nature, 158, 339

Savolainen T., Wiik K., Valtaoja E., Jorstad S. G., Marscher A. P., 2002, A&A, 394, 851

Schmidt M., 1963, Nature, 197, 1040

Schwab F. R., 1984, AJ, 89, 1076

Schwab F. R., Cotton W. D., 1983, AJ, 88, 688

Seyfert C. K., 1943, ApJ, 97, 28

Shakura N. I., Sunyaev R. A., 1973, A&A, 24, 337

Shapiro S. L., Teukolsky S. A., 2004, Black holes, white dwarfs, and neutron stars: The physics of compact objects, 2nd edn. Wiley-VCH

Shepherd M. C., Pearson T. J., Taylor G. B., 1994, in Bulletin of the American Astronomical Society, Vol. 26, Bulletin of the American Astronomical Society, pp. 987–989

Sholomitskii G. B., 1965a, AZh, 42, 673

Sholomitskii G. B., 1965b, Soviet Ast., 9, 516

Sikora M., Begelman M. C., Madejski G. M., Lasota J., 2005, ApJ, 625, 72

Sikora M., Begelman M. C., Rees M. J., 1994, ApJ, 421, 153

Sillanpää A., Haarala S., Valtonen M. J., Sundelius B., Byrd G. G., 1988, ApJ, 325, 628

Spencer R., 2005, Highlights of Astronomy, 13, 709

Steer D. G., Dewdney P. E., Ito M. R., 1984, A&A, 137, 159

T. Belloni, ed., 2010, Lecture Notes In Physics, Vol. 794, The Jet Paradigm: From Microquasars to Quasars. Springer

Thompson A. R., Moran J. M., Swenson, Jr. G. W., 2004, Interferometry and Synthesis in Radio Astronomy, 2nd edn. Wiley-VCH

Urry C. M., Padovani P., 1995, PASP, 107, 803

Valtaoja E., Terasranta H., Urpo S., Nesterov N. S., Lainela M., Valtonen M., 1992, A&A, 254, 71

Vitrishak V. M., 2008, PhD thesis, Moscow State University, in Russian

Vitrishchak V. M., Gabuzda D. C., Algaba J. C., Rastorgueva E. A., O'Sullivan S. P., O'Dowd A., 2008, MNRAS, 391, 124

Vlahakis N., Königl A., 2004, ApJ, 605, 656

Wagner S. J., Witzel A., 1995, ARA&A, 33, 163

Wakker B. P., Schwarz U. J., 1988, A&A, 200, 312

Wardle J. F. C., Homan D. C., 2003, Ap&SS, 288, 143

Wardle J. F. C., Homan D. C., Ojha R., Roberts D. H., 1998, Nature, 395, 457

Whitney A. R. et al., 1971, Science, 173, 225

Wilson T. L., Rohlfs K., Hüttemeister S., 2009, Tools of Radio Astronomy, 5th edn. Springer

My contributions to the publications

Paper I: Evidence for cospatial optical and radio polarized emission in active galactic nuclei.
Data reduction, analysis, contribution to text writing.

Paper II: Multi-frequency VLBA study of the blazar S5 0716+714 during the active state in 2004. I. Inner jet kinematics.
Data reduction, analysis, and text writing.

Paper III: Multifrequency VLBA study of the blazar S5 0716+714 during the active state in 2004. II. Large-scale jet kinematics and the comparison of the different methods of VLBI data imaging as applied to kinematic studies of AGN.
Idea, data reduction, analysis, and text writing.

Paper IV: The 15-43 GHz parsec-scale circular polarization of 41 active galactic nuclei.
Contribution to data reduction and text writing.

Paper V: Multifrequency VLBA study of the blazar S5 0716+714 during the active state in 2004.III. Detection of the variable circular polarization on the parsec scale.
Idea, data reduction, analysis, and text writing.